The Astrophysical Journal, 871:206 (18pp), 2019 February 1 https://doi.org/10.3847/1538-4357/aafa1a

# Following the Cosmic Evolution of Pristine Gas. III. The Observational Consequences of the Unknown Properties of Population III Stars

Richard Sarmento[1], Evan Scannapieco[1], and Benoit Côté[2,3,4]

[1] School of Earth and Space Exploration, Arizona State University, P.O. Box 871404, Tempe, AZ 85287-1404, USA
[2] National Superconducting Cyclotron Laboratory, Michigan State University, Lansing, MI 48823, USA
[3] Konkoly Observatory, Research Centre for Astronomy and Earth Sciences, Hungarian Academy of Sciences, Konkoly Thege Miklos ut 15-17, H-1121 Budapest, Hungary
[4] Joint Institute for Nuclear Astrophysics—Center for the Evolution of the Elements

*Received 2018 August 9; revised 2018 December 18; accepted 2018 December 18; published 2019 February 1*

## Abstract

We study the observational consequences of several unknown properties of Population III stars using large-scale cosmological simulations that include a subgrid model to track the unresolved mixing of pollutants. Varying the value of the critical metallicity that marks the boundary between Population III and Population II star formation across 2 dex has a negligible effect on the fraction of Population III stars formed and the subsequent fraction of Population III flux from high-redshift galaxies. However, adopting a lognormal initial mass function (IMF) for Population III stars, in place of a baseline Salpeter IMF, results in a Population III star formation rate density that is $1/4$ of the baseline rate. The flux from high-redshift galaxies modeled with this IMF is highly bimodal, resulting in a tiny fraction of $z \leqslant 8$ galaxies with more than 75% of their flux coming from Population III stars. However, at $z = 9$, right before reionization in our simulations, $\approx$20% of galaxies are Population III-bright with $m_{\mathrm{UV}} \leqslant 31.4$ mag, and at least 75% of their flux is generated by Population III stars. Additionally, the lognormal Population III IMF results in a population of carbon-enhanced, metal-poor stars in reasonable agreement with MW halo observations. Our analysis supports the conclusion that the Population III IMF was dominated by stars in the 20–120 $M_{\odot}$ range that generate supernovae with carbon-enhanced ejecta.

*Key words:* cosmology: theory – early universe – galaxies: high-redshift – evolution – stars: formation – Population III

## 1. Introduction

Many of the characteristics of the first stars are uncertain (Bromm et al. 1999; Abel et al. 2000; Norman 2010), but it is likely that they began to form at $z \approx 20$ in minihalos with total masses $\sim 10^6$ $M_{\odot}$ (Abel et al. 2002; Bromm et al. 2002). Since $H_2$ was the only available coolant in the primordial gas, fragmentation was likely mostly suppressed, giving rise to an initial mass function (IMF) that was likely biased toward massive stars (Tumlinson 2006; Brook et al. 2007; Salvadori et al. 2010; Susa et al. 2014).

The shape and characteristic mass of the Population III IMF are still unknown, although estimates of the likely maximum mass of such stars have been decreasing in recent years (Whalen 2012; Susa 2013; Susa et al. 2014; Ishigaki et al. 2018). Early modeling efforts estimated the mass of the first Population III stars at 100–500 $M_{\odot}$ (Bromm et al. 1999, 2001; Abel et al. 2000, 2002). More recent estimates point to an IMF in the range of 30–300 $M_{\odot}$ (O'Shea & Norman 2007). However, there is now evidence from numerical simulations of primordial protostellar clouds that the very first Population III stars did not necessarily form solely as single stars or binaries. Instead, the protostellar accretion disk may have fragmented, resulting in the birth of several Population III stars from a primordial natal cloud with masses of order 10 $M_{\odot}$ (Turk et al. 2009; Johnson 2010; Stacy et al. 2010; Clark et al. 2011; Stacy & Bromm 2013, 2014).

Although there have been several efforts to find Population III stars in and around the Galaxy, as well as in early galaxies at high redshift, observational efforts have yet to discover this first generation of stars (Nagao et al. 2008; Kashikawa et al. 2012; Cassata et al. 2013; Sobral et al. 2015). Given the lack of observations of Population III stars, it has fallen to theory and simulation to derive some of their characteristics. While theoretical studies have become more sophisticated (Mackey et al. 2003; Scannapieco et al. 2003; O'Shea & Norman 2007; Tornatore et al. 2007; Norman 2010; Wise et al. 2011; Johnson et al. 2013; Hartwig et al. 2014; Pallottini et al. 2014; Xu et al. 2016a; Jaacks et al. 2018), they have to make simplifying assumptions and choices for several of the relevant parameters surrounding star formation and supernova (SN) feedback given the scales required to model a statistically significant volume in the early universe.

The most important of these are likely to be (1) the critical metallicity that marks the boundary between Population III and Population II star formation and (2) the efficiency of Population III SN feedback that determines how metals from the first stars are disseminated. The critical metallicity is believed to be between $10^{-6}$ and $10^{-3}$ $Z_{\odot}$ depending on how efficiently dust can act to radiatively cool the gas (Dopcke et al. 2011; Schneider et al. 2012; Dopcke et al. 2013). Its value has direct implications for Population III star formation since it dictates which parcels of gas form Population III stars. The energy generated by Population III SNe (Kitayama & Yoshida 2005; Smidt et al. 2014), on the other hand, is tightly coupled to the Population III IMF, which determines the fraction of stars that generate SNe and the energies with which they eject metals.

Together these unknown properties have important implications for the two main methods used to constrain Population III star formation: direct searches and analyses of extremely metal-poor (EMP) stars. While direct measurements of individual Population III stars at high redshift are challenging (Windhorst et al. 2018), dwarf galaxies containing these stars are expected to display several unique signatures. Population III stars are predicted to be very blue, not only because they are likely to be massive but also because they have lower opacities and higher core temperatures (Castellani et al. 1983; El Eid et al. 1983). This leads to stronger UV emission, inducing strong nebular Ly$\alpha$ emission (Bromm et al. 2001; Schaerer 2002), as well as nebular He II $\lambda$1640 emission, which is one of the most promising Population III tracers (Tumlinson & Shull 2000; Tumlinson et al. 2001; Panagia et al. 2003).

A complementary approach to constraining the properties of the first stars is to analyze their fossil remnants. While Population III stars themselves are not expected to last until the present day, the elements they ejected should remain preserved in low-metallicity, second-generation stars, unmixed with material from later populations. These second-generation stars are rare overall but are expected to make up a substantial fraction of metal-poor stars (Freeman & Bland-Hawthorn 2002; Frebel et al. 2005; Frebel & Norris 2015). Of particular interest are CEMP-no[5] stars, carbon-enhanced metal-poor (CEMP) stars that do not display an enhancement of *r*- or *s*-process elements (Beers & Christlieb 2005). Such stars are likely polluted by a single or at most a few Population III SNe. Their unusual abundances argue for a Population III IMF with a characteristic mass of order tens of solar masses (Keller et al. 2014; Hartwig et al. 2015; de Bennassuti et al. 2017; Ishigaki et al. 2018). If this is true, the overall Population III rate of Type II SNe would be significantly higher than that of stars today (Heger & Woosley 2002; Woosley et al. 2002; Whalen et al. 2013).

In Sarmento et al. (2017, hereafter Paper I), we attempted to identify a characteristic Population III mass by comparing the SN nucleosynthetic yields of Population III stars to the chemical abundances measured in a subset of carbon-enhanced, metal-poor Milky Way (MW) halo stars. In Sarmento et al. (2018, hereafter Paper II), we characterized the high-redshift luminosity function (LF; Mason et al. 2015; O'Shea et al. 2015), making predictions for the *James Webb Space Telescope* (*JWST*). Both these studies used a value near the middle of the range for the critical metallicity, $Z_{\rm crit} = 10^{-5}$, along with typical SN rates and energies for stellar masses drawn from a Salpeter (1955) IMF[6]. All Population III SN yields were assumed to be from a 60 $M_\odot$ Population III star (Heger 2018).

In this work, we vary several of the parameters discussed above, evaluate the implications against our previous results, and compare them to observations of CEMP-no stars. In particular, we investigate the effects of the value of the critical metallicity on the transition from Population III to Population II star formation. We implement a lognormal IMF, within our simulation, for Population III stars that significantly changes the amount of SN feedback and the fraction of surviving Population III stars after $\approx$10 Myr. We also examine the effects of different SN mass loading on subsequent Population III star formation.

This paper is structured as follows. In Section 2 we describe our methods, including a brief review of our implementation of the subgrid model tracing the fraction of pristine gas, some of the relevant physics modeled, and the setup for the simulations used in this parameter study. In Section 3 we discuss our results and the effects of the various parameters on the high redshift luminosity function (LF), the fraction of Population III flux emitted by early galaxies, and the subsequent effect on the chemical composition of Population II stars. Finally, conclusions are discussed in Section 4.

## 2. Methods

In this section, we review the simulation methods and parameter choices for the runs discussed in this work. The physics, cosmology, and implementation of the pristine gas fraction scalar, as well as the primordial metallicity scalar, are described in more detail in Paper I.

### 2.1. Simulation Setup

To facilitate comparisons with Paper I and Paper II, we adopted the cosmological parameters used therein: $\Omega_{\rm M} = 0.267$, $\Omega_\Lambda = 0.733$, $\Omega_{\rm b} = 0.0449$, $h = 0.71$, $\sigma_8 = 0.801$, and $n = 0.96$, based on Komatsu et al. (2009). These parameters have their usual cosmological definitions.

We again made use of RAMSES (Teyssier 2002), an adaptive mesh refinement (AMR) cosmological simulation code, to model a 12 Mpc $h^{-1}$ on-a-side volume generated from Multi-Scale Initial Conditions (MUSIC; Hahn & Abel 2013). We evolved this volume to $z = 7$ covering approximately the first 780 Myr of cosmic history, given our cosmology, for each of the new simulations analyzed.

The following parameters are common to all of the simulations discussed in this work. The initial grid resolution of 11.7 comoving kpc $h^{-1}$ was based on a starting resolution of $1024^3$ cells ($l_{\rm min} = 10$). Our choice for the initial resolution resulted in a dark matter (DM) particle mass of $4.47 \times 10^5 M_\odot$ $h^{-1}$ $\Omega_{\rm DM}$ or $1.40 \times 10^5$ $M_\odot$ for our cosmology.

We took a quasi-Lagrangian approach to refinement. As cells became overdense, RAMSES refined them to ensure that the mean mass per cell was roughly constant across the simulation. We allowed for up to eight additional refinement levels ($l_{\rm max} = 18$); however, the highest refinement level reached by $z = 7$ was $l = 15$, resulting in a best physical resolution of 64.5 pc.

We did not model black holes (BHs), since their feedback is likely not important for high-redshift galaxy evolution (Scannapieco & Oh 2004; Somerville et al. 2008; Jeon et al. 2012; Prieto et al. 2017), the galaxy mass range explored, or the parameters we are interested in investigating. The redshift of reionization was also a free parameter, which we set to $z_{\rm re} = 8.5$, as reported by Planck Collaboration et al. (2016). Reionization is a discrete event in the simulation.

### 2.2. Simulation Physics

RAMSES uses CLOUDY (Ferland et al. 1999) to model atomic/ionic cooling for $T \gtrsim 10^4$ K. We used the cooling rates from Rosen & Bregman (1995) for temperatures below this value. We set the radiative cooling floor to 100 K, but adiabatic cooling can lower the gas temperature below this value. The UV background was derived from Haardt & Madau (1996).

As discussed in Paper I, we also modeled molecular cooling in the pristine gas (Johnson & Bromm 2006; Prieto et al. 2008; Hirano & Yoshida 2013). Our analytic model is based on work by Martin et al. (1996) and provides a radiative cooling rate, $\Lambda_r/n_{\rm H_2}$, for the gas densities encountered in the simulations. We

---

[5] CEMP-no: [Fe/H] $< -1.0$, [C/Fe] $> +0.7$ and [Ba/Fe] $< 0.0$.

[6] While SN rates were based on a Salpeter IMF, the flux from the surviving stars was modeled, in post-processing, using a lognormal IMF. This model mismatch is addressed in this work.

assumed a primordial $H_2$ fraction of $10^{-6}$ (Reed et al. 2005) and an optically thin simulation box. As a result, all of our $H_2$ is destroyed shortly after the first stars are formed since they produced more Lyman–Werner photons than there were $H_2$ molecules in our simulation volume. We did not model $H_2$ formation.

The simulations spawned star particles (SPs) in regions of gas according to a Schmidt law (Schmidt 1959) using a star formation rate

$$\frac{d\rho_\star}{dt} = \epsilon_\star \frac{\rho}{t_{\rm ff}}, \text{ when } \rho > \rho_{\rm th}, \tag{1}$$

where $t_{\rm ff} = \sqrt{3\pi/(32G\rho)}$ is the gas freefall time. Star-forming regions also needed to be at least 200 times the mean density of the simulation, as a function of redshift, before SPs were formed. This ensured that SPs were only formed in collapsed objects and not in high-density flows (Rasera & Teyssier 2006; Dubois & Teyssier 2008).

For our simulations we set $\rho_{\rm th} = 1.0\, H\ {\rm cm}^{-3}$ and the star-forming efficiency to $\epsilon_\star = 0.01$, giving results in reasonable agreement with the observed high-redshift star formation rate (Madau & Dickinson 2014; Finkelstein 2016). Our SP mass resolution was

$$m_\star = \frac{\rho_{\rm th}}{X} \Delta x_{\rm min}^3 = 8.6 \times 10^3\ M_\odot, \tag{2}$$

where we account for a primordial H fraction of $X = 0.76$. The final mass of each SP was drawn from a Poisson process such that it was a multiple of $m_\star$.

The range of SP masses generated across the simulations was $8.6 \times 10^3\ M_\odot \leqslant M_\star \leqslant 6.0 \times 10^4\ M_\odot$. When considering our lognormal IMF and the minimum SP mass, we sampled 62 stars in the mass range of 20–120 $M_\odot$, composing a total mass of $\approx 3580\, M_\odot$ per SP. Additionally, all of our star-forming galaxies at $z \leqslant 16$ generated at least four SPs per halo. The nonlinear length scale at the end of the simulations, $z = 7$, was 47 comoving kpc $h^{-1}$. This scale corresponds to a mass of $3.2 \times 10^7\, M_\odot\ h^{-1}$.

Each SP formed prompts an SN event after 10 Myr. This SN represents the stars with masses greater than approximately 16 $M_\odot$ in the IMF. We note that all of our SN feedback occurred after 10 Myr even though many of the very high mass stars would have had much shorter lives. Further, each SN injected $E_{\rm SN} = 10^{51}$ erg/10 $M_\odot$ in the form of kinetic energy of the gas.

Radiation pressure from Population III and other massive stars can disrupt—and also trigger—star formation (Whalen et al. 2004; Deharveng et al. 2010; Wise et al. 2011; Tremblin et al. 2012), affecting the star formation rate in high-redshift galaxies; we did not include its effects in this work.

### 2.3. The Pristine Fraction, Corrected Metallicity, and the Primordial Metallicity

For these simulations, we made use of the modifications to RAMSES described in Paper I to track two new metallicity-related scalars. These allowed us to more accurately model the fraction of Population III stars created in high-redshift galaxies and to follow the unique elemental yields generated by Population III SNe. The *pristine gas mass fraction*, $P$, and the *primordial metallicity*, $Z_P$, are described below. Additionally, we discuss how we used the pristine fraction to improve the accuracy of the metallicity of the polluted fraction of gas and SPs.

#### 2.3.1. The Pristine Fraction

The pristine gas fraction, $P$, was used to track the mass fraction of gas with $Z < Z_{\rm crit}$ in each simulation cell. The scalar evolves from $P = 1$, indicating that 100% of the gas in the cell is metal-free, to $P = 0$, indicating that all of the gas in the cell has been polluted above $Z_{\rm crit}$. $P_\star$ records the value of $P$ in SPs at the time they were spawned and identifies the mass fraction of Population III stars with $Z_\star < Z_{\rm crit}$ for each SP.

As discussed in detail in Pan et al. (2013) and first implemented in a cosmological simulation in Paper I, the following equation was used to describe the evolution of the pristine gas fraction:

$$\frac{dP}{dt} = -\frac{n}{\tau_{\rm con}} P(1 - P^{1/n}). \tag{3}$$

The change in the pristine gas fraction at each time step was therefore a function of $n$, a measure of the locality of mixing, and a timescale, $\tau_{\rm con}$, that is the inverse of the turbulent stretching rate (Pan & Scannapieco 2010; Pan et al. 2012, 2013). These parameters are, in turn, functions of the turbulent Mach number, $M$, and the average metallicity of the cell relative to the critical metallicity, $\overline{Z}/Z_{\rm crit}$ (Paper I). By knowing $P$ at the time of star formation, we subsequently modeled the mass fraction of Population III stars for each SP formed as $M_{\star,{\rm III}} = M_\star \times P_\star$.

#### 2.3.2. The Corrected Metallicity

Each SP in the simulation recorded both the host cell's average metallicity, $\overline{Z} \rightarrow \overline{Z}_\star$, and the pristine gas fraction, $P \rightarrow P_\star$, at the time it was created. This information was combined to model the metallicity of the polluted fraction of gas or stars. When metals were well mixed throughout the cell's volume, $P = 0$ and the scalar $\overline{Z}$ represented the average metallicity of any subvolume of gas in the cell. However, before mixing was completed, the polluted fraction, $f_{\rm pol} \equiv 1 - P$, described the fraction of gas that was actually polluted with metals. Therefore, a better estimate of the metallicity of the polluted fraction of gas was the *corrected metallicity*,

$$Z = \frac{\overline{Z}}{f_{\rm pol}}. \tag{4}$$

As expected, when $f_{\rm pol} = 1$, the corrected metallicity was the average metallicity. However, when $f_{\rm pol} < 1$, only a fraction of the cell was polluted, and the metals were concentrated in a volume smaller than the cell and hence $Z > \overline{Z}$ for that fraction of gas. When referring to the corrected metallicity of the polluted fraction of gas or SPs, we use $Z$ or $Z_\star$.

As discussed in Paper I, the corrected metallicity was precise only when all of the metals in the cell are contained in the polluted fraction. However, it is possible for the gas in a cell to have been uniformly polluted to $0 < \overline{Z} < Z_{\rm crit}$ via advection or mixing of dilute metals from a previous SN. Such cells are still capable of creating Population III stars. When material from a new SN entered such a cell, the polluted fraction, $f_{\rm pol}$, did not represent all of the metals in the cell.

Equation (4) accurately models the metallicity of the polluted fraction of gas when the unpolluted fraction has $\overline{Z} = 0$. This equation is therefore the upper bound to the metallicity of the polluted fraction. A lower bound to the corrected metallicity, for the situation described above, is reached when the maximum fraction of metals is already well mixed in a cell but the cell is just below $Z_{\mathrm{crit}}$. When new pollutants entered such a cell, it resulted in the metallicity of the polluted fraction

$$Z = \frac{\overline{Z} - Z_{\mathrm{crit}}}{f_{\mathrm{pol}}}, \tag{5}$$

where $Z_{\mathrm{crit}} = \{10^{-6}, 10^{-5}, 10^{-4}\} Z_{\odot}$ (for runs Z6, fid, and Z4, respectively). This equation accounts for metals in the pristine fraction of gas. Note that when we set $Z_{\mathrm{crit}} = 0$, representing a cell with purely primordial gas in its pristine fraction, Equation (5) becomes Equation (4) as we would expect. Given the small amount of metals that could be mixed in the pristine fraction, we ignore this effect for cells that had a pristine fraction $0 < \overline{Z} < Z_{\mathrm{crit}}$.

Finally, we did not create polluted stars when $f_{\mathrm{pol}} < 10^{-5}$. This limit had no impact on our final results even though imposing it could have theoretically resulted in a tiny fraction of highly enriched SPs. However, the maximum metallicity reached for any SP in the simulation was $0.36\,Z_{\odot}$ at $z = 7$.

### 2.3.3. Primordial Metals

We refer to the metals generated by the first stars as *primordial metals*. Since the elemental abundance patterns for ejecta from massive Population III SNe are likely different from those of lower-mass Population II stars (Heger & Woosley 2002), we developed a straightforward method to track these metals in a cosmological simulation. Anytime an SP with a nonzero pristine fraction went SN, we tracked the Population III SN ejecta with the scalar $\overline{Z}_{\mathrm{P}}$.

This new scalar allowed us to follow primordial metals injected into the gas and to model the final metal content of subsequently formed SPs. Once we applied our correction to the metallicity, the fraction of primordial metals in SPs was computed as $Z_{\mathrm{P},\star}/Z_{\star}$, where $Z_{\star}$ captures the total metallicity of the SP. When mapping these metallicities to the chemical composition of an SP (or fraction thereof for $0 < P < 1$), we used $Z_{\star} - Z_{\mathrm{P},\star}$ to model the mass fraction of "normal" metals, while $Z_{\mathrm{P},\star}$ modeled the mass fraction of primordial metals produced by a representative Population III SN abundance pattern or integrated Population III IMF SN yields.

## 2.4. Simulations

We carried out a set of five large-scale cosmological simulations to study the effects of varying the critical metallicity, SN mass loading, and Population III IMF on the star formation rate, the luminosity of galaxies, and the fraction of Population III flux coming from them. Table 1 identifies the simulations and their corresponding parameters. Note that the fid and fid_orig runs use the same simulation output; the only difference is the IMF used to model surviving (post-SN) SP mass. All other simulation parameters were consistent across all runs, as described in Section 2.1 and captured in Table 2.

We include comparisons to the simulation in Paper II, fid_orig, that used a lognormal IMF to model the spectral energy density (SED) of Population III stars in post-processing, even though the surviving post-SN SP mass fraction, after 10 Myr, was representative of a Salpeter IMF.

**Table 1**
Simulation Parameters

| Name | $Z_{\mathrm{crit}}$ | $f_w$[a] | Population III IMF | $\alpha$ | $M_{\mathrm{c}} / M_{\odot}$ | $\sigma$ |
|---|---|---|---|---|---|---|
| fid | $10^{-5}$ | 10 | Salpeter[b,c] | 2.35 | ⋯ | ⋯ |
| Z4 | $10^{-4}$ | 10 | Salpeter[b] | 2.35 | ⋯ | ⋯ |
| Z6 | $10^{-6}$ | 10 | Salpeter[b] | 2.35 | ⋯ | ⋯ |
| P3SN | $10^{-5}$ | 10 | Lognormal[d] | ⋯ | 60 | 1.0 |
| fw1 | $10^{-5}$ | 1 | Salpeter[b] | 2.35 | ⋯ | ⋯ |
| fid_orig | $10^{-5}$ | 10 | Lognormal[c,d] | ⋯ | 60 | 1.0 |

**Notes.**
[a] SN mass loading. The amount of gas, expressed in multiples of the mass of SN ejecta, carried along with the SN blast and removed from the host cell.
[b] The Salpeter IMF mass range spans 0.6–100 $M_{\odot}$.
[c] Both fid and fid_orig are based on the same RAMSES simulation data. However, for fid the SEDs used to model Population III flux in post-processing assumed a lognormal IMF for SP mass; the fid_orig results assumed a Salpeter IMF.
[d] The lognormal IMF mass range spans 1–500 $M_{\odot}$.

**Table 2**
Common Simulation Parameters

| Name | Value | Name | Value |
|---|---|---|---|
| $\Delta x_{\mathrm{min}}$ | 64.5 pc | $\rho_{\mathrm{th}}$ | 1 H cm$^{-3}$ |
| $M_{\mathrm{DM}}$ | $1.4 \times 10^{5}\ M_{\odot}$ | $E_{\mathrm{SN}}$ | $10^{51}$ erg/10 $M_{\odot}$ |
| $m_{\star}$ | $8.6 \times 10^{3}\ M_{\odot}$ | $z_{\mathrm{re}}$ | 8.5 |
| $r_{\mathrm{bubble}}$ | 300 pc | SN $Z$ yield[a] | 0.15 |

**Note.**
[a] The mass fraction of metals produced by SNe.

The critical metallicity, $Z_{\mathrm{crit}}$, marks the boundary between Population III and Population II star formation. This parameter is loosely constrained (Omukai et al. 2005), and we explored the effects of varying the critical metallicity across 2 orders of magnitude. We defined the critical metallicity of the gas for the fiducial (fid) run as $Z_{\mathrm{crit}} = 10^{-5}\,Z_{\odot}$, as was done in our earlier works (fid_orig). The runs Z4 and Z6 were used to determine the effects of setting the critical metallicity 1 dex higher and lower, respectively.

By default, the RAMSES model for stellar evolution assumes that a user-specified fraction, $\eta_{\mathrm{SN}}$, of the mass of each SP, regardless of the SP's metallicity or pristine fraction, goes SN after 10 Myr. We used $\eta_{\mathrm{SN}} = 0.10$ for the fid, Z4, Z6, fw1, and fid_orig runs corresponding to the massive, short-lived stars at the top of a Salpeter (1955) IMF with a mass range of 0.6–100 $M_{\odot}$.

For this study we implemented a second IMF for Population III stars within the simulation. The fraction of each SP, in run P3SN, with metallicity below $Z_{\mathrm{crit}}$ is $P_{\star} \times M_{\star}$ and was modeled using a lognormal Population III IMF (Larson 1973; Tumlinson 2006; Raiter et al. 2010). Our Population III IMF had a characteristic mass of 60 $M_{\odot}$ and $\sigma = 1$. The mass range spanned 1–500 $M_{\odot}$ and corresponds to Model ID "TE" in Raiter et al. (2010). Specifically, our IMF was

$$\frac{dN}{d\,\ln M} = \exp\left[-0.902 - \frac{1}{2\sigma^{2}} \ln\left(\frac{M}{60\,M_{\odot}}\right)^{2}\right], \tag{6}$$

where $-0.902$ normalizes the probability density function (pdf).

Our Population III IMF resulted in 99% ($\eta_{\mathrm{SN,III}} = 0.99$) of the stars going SN within the first 10 Myr (Heger & Woosley 2010), representing a significant increase in feedback energy and the amount of metals injected into the ISM as compared to the fiducial case. Note that we used the same Type II SN fractional metal yield and explosion energy for all Population III SNe in this IMF, although a subset of stars in the mass range 40–140 $M_\odot$ may collapse directly into BHs, while higher-mass stars likely generate pair-instability SNe with different explosion energies and yields (Heger et al. 2003; Scannapieco et al. 2005). We leave the exploration of this parameter space to a future work.

Still considering run P3SN, the fraction of Population II stars, per SP, had mass $(1.0 - P_\star) \times M_\star$. This IMF was modeled using the Salpeter IMF described above with $\eta_{\mathrm{SN}} = 0.10$. The Population II IMF used the standard power-law slope, $\alpha = 2.35$.

As mentioned above, all SNe in the simulation injected $E_{\mathrm{SN}} = 10^{51}$ erg/10 $M_\odot$ as kinetic energy (Dubois & Teyssier 2008). Further, we assumed that 15% of SN ejecta, by mass, were metals, regardless of the type of SP.

The mass-loading parameter, $f_w$, established the amount of gas, in terms of a multiple of the mass of SN ejecta, in the host cell that was carried along with the SN blast. For this work and our previous studies, we used a default value of $f_w = 10$. This material was subsequently distributed equally among all of the cells within the SN blast radius of 300 pc, or a volume of $\approx 1.13 \times 10^8$ pc$^3$. For this study, we explored the effect of reducing the mass-loading factor to $f_w = 1$ via run fw1.

While the fractional difference in the amount of material carried into the cells in the SN blast radius was insignificant, reducing $f_w$ from 10 to 1 resulted in high-redshift galaxies retaining more of their gas. Specifically, for the $f_w = 10$ fiducial case, each SN removed 1 SP mass of gas, at least $8.6 \times 10^3\,M_\odot$, from the host cell since the SN ejecta mass was 10% of the SP mass. This helped to modulate future star formation by reducing the gas in star-forming cells, although, for numerical reasons, the maximum amount of gas carried by any SN was capped at 25% of the gas remaining in the host cell. For $f_w = 1$, 10× more gas was left in the central star-forming region of active galaxies as compared to the fiducial case, assuming that the 25% limitation was not routinely reached.

### 2.5. Halo Finding

AdaptaHOP (Aubert et al. 2004) was used to find star-forming galaxies in the simulation. Groups of 20 particles were used to compute the local matter density, and halos must have been composed of at least 100 DM particles, equivalent to a DM halo mass of $1.4 \times 10^7\,M_\odot$, to have been considered a candidate halo. Further, only candidates with densities 80 times the average total matter density, as a function of redshift, were stored.

Many of the more massive objects found by AdaptaHOP were composed of more than one observationally distinguishable galaxy, and these overly bright objects had the potential to bias the bright end of our LFs. To determine the radius of observationally distinguishable galaxies, we post-processed them as described in Paper II. Our method assumed an *HST*-like criterion for separability of sources and required at least a $0.1''$ separation between objects. The vast majority of these objects were too dim to detect in unlensed *JWST* fields. However, they did provide information at the faint end of our LFs.

### 2.6. Galaxy Spectral Models and Simulated Observations

We computed the UV fluxes, at a rest-frame wavelength of 1500 Å, for our simulated galaxies based on the redshift, ages, metallicities, and masses of their constituent SPs using a set of simple stellar population SED models as was done in Paper II. Our original study, fid_orig, modeled the flux from all Population III stars with $Z_\star < Z_{\mathrm{crit}}$ using $Z_\star = 0$ SEDs using a lognormal IMF to interpret SP mass. This was in tension with the Salpeter IMF modeled in the simulation. While we pointed this out in the original work, we correct this mismatch by using SEDs based on a Salpeter IMF for new runs that use 10% as the SN fraction for SPs. This fraction corresponds to the massive stars at the top of a Salpeter IMF. This includes runs fw1, fid, Z4, and Z6. For run P3SN we use the lognormal SED for Population III SPs that agrees with the 99% of SP mass that goes SN after 10 Myr.

Each of the model SEDs was redshifted over the range $z = 7$–16 and attenuated to account for Lyman forest and continuum absorption (Madau 1995). This process also included a spectral conversion from wavelength to frequency converting the SEDs into the familiar units of flux, normalized to an IMF of stars with 1 solar mass: erg/s/Hz/cm$^2$/$M_\odot$. As in our previous work, we did not consider attenuation due to dust.

All of the SEDs, translated into fluxes at a given redshift, modeled stars of discrete metallicities and discrete ages spanning the age range of SPs in the simulation. We interpolated the data in both metallicity and age linearly, in log-space, to determine the flux of specific SPs and fractions thereof.

Specifically, the fluxes for all Population II SPs, for all runs, were based on an SED with a Salpeter IMF normalized to 1 $M_\odot$. The fluxes were derived from *STARBURST99* SEDs (Leitherer et al. 2014), supplemented with SEDs by Raiter et al. (2010), for $Z_{\mathrm{crit}} \leqslant Z_\star \leqslant 5 \times 10^{-4}\,Z_\star$.

Population III SPs, with $Z_\star < Z_{\mathrm{crit}}$, had fluxes that were based on Raiter et al. (2010) SEDs for a stellar population with $Z_\star = 0$. For runs fid, fw1, Z4, and Z6 the SEDs modeled a Salpeter IMF. Run P3SN used a Population III SED modeled on the lognormal IMF described in Table 1. Once again, these SEDs were normalized to an IMF of 1 $M_\odot$ that made it straightforward to scale the flux by the mass of the SPs.

## 3. Results

We analyze our simulations with a focus on Population III stars both in aggregate and within the context of galaxies, focusing on $7 \leqslant z \leqslant 15$. Figure 1 depicts the star formation rate density (SFRD) for our simulations, along with observational data compiled by Madau & Dickinson (2014) and Finkelstein (2016). Our SFRDs are in reasonable agreement with the LF-based SFRD described by Finkelstein (2016) over the range $7 \leqslant z \leqslant 8$ when considering both Poisson error and sample variance (Trenti & Stiavelli 2008). To minimize parameter differences between runs, we use the same star-forming efficiency for all runs. We include the 1$\sigma$ estimated errors only for the fid and P3SN runs since they show the

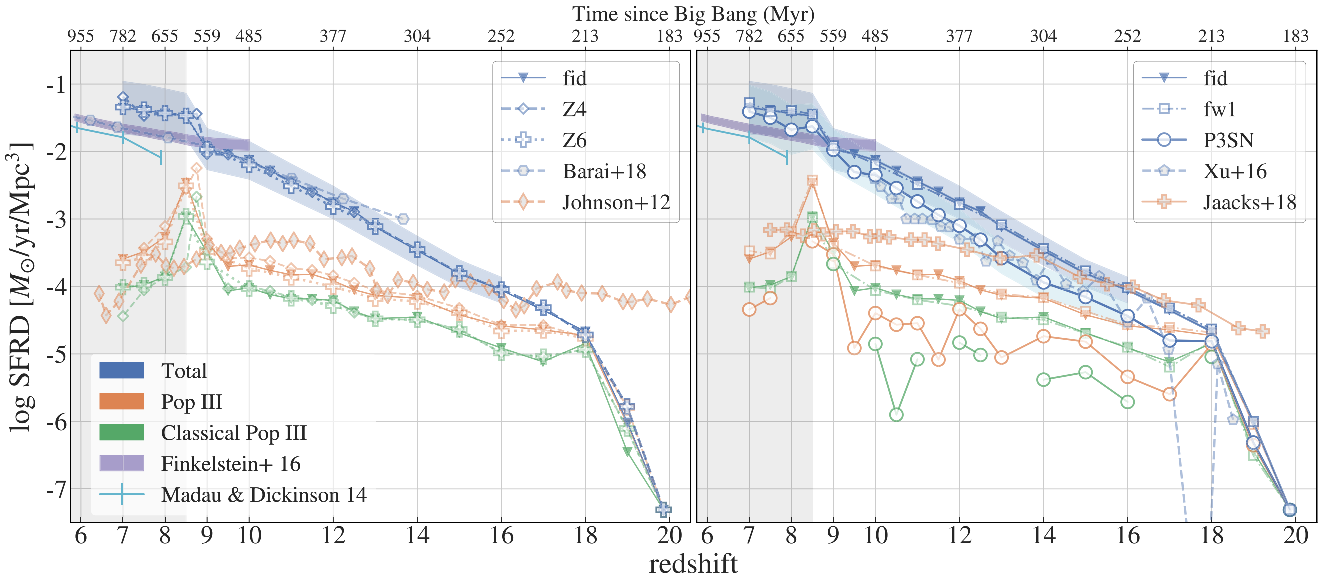

**Figure 1.** SFRDs for our simulations and, for comparison, from Barai & de Gouveia Dal Pino (2018) and Xu et al. (2016b), along with a compilation of observations by Madau & Dickinson (2014). We also include an LF-derived SFRD by Finkelstein (2016), based on an integration of the reference's LF to $M_{\rm UV} = -13$ mag. The $1\sigma$ uncertainties on the fid and P3SN runs (light-blue shading) at $z \leqslant 16$ account for both Poisson noise and sample variance. We include two Population III SFRDs for each of our simulations. The "Population III" (orange) rate includes the effects of the subgrid model when determining the fraction of Population III stellar mass. The "classical Population III" (green) rate only includes Population III SPs that are formed in cells with $Z < Z_{\rm crit}$. Population III SFRDs by Jaacks et al. (2018) and Johnson et al. (2013) are also in orange. The Population III SFRDs show very little variation over 2 orders of magnitude of the critical metallicity (runs Z4 and Z6). The largest effect on the star formation rate occurs when changing the IMF for Population III stars: run P3SN. The Population III SFRD for run P3SN is ≈0.23 of the fid rate owing to both increased feedback from the Population III IMF and the smaller surviving fraction of Population III stars. The gray shaded area indicates redshifts post-reionization. If data are missing for a redshift, this indicates an SFRD of zero.

greatest variation in the SFRD between simulations. For a detailed discussion on error estimation see Paper II.

Figure 1 also depicts the Population III SFRD, as well as the "classical" Population III SRFD that does not include the effects of our subgrid model. The "Population III" rate uses $P_\star \times M_\star$ to compute Population III stellar mass. The "Classical Population III" rate only considers whole SPs where $\overline{Z_\star} < Z_{\rm crit}$ and hence requires $P_\star = 1.0$ for an SP's mass to be included in the classical SFRD. The three runs with different critical metallicities, $Z_{\rm crit}/Z_\odot = \{10^{-4}, 10^{-5}, 10^{-6}\}$, do not show much variation in the Population III rate.

However, the variation due to modeling the evolution of the pristine gas fraction, $P$, accounts for an average increase of a factor of ≈2 (0.3 dex) in the Population III SFRD, at $z < 18$, as compared to the classical rate, when averaged across all five runs. This demonstrates that modeling the subgrid unpolluted fraction of gas is more important than knowing the critical metallicity when attempting to predict the Population III star formation rate.

Comparing the Population III SFRDs, the greatest change is caused by the change to the Population III IMF in run P3SN. This is not surprising since the lognormal IMF adopted for Population III stars results in ≈10× more SN energy and pollutants, as well as ≈90% less mass in surviving Population III SPs after 10 Myr, as compared to the other runs. The fid run's Population III SFRD is approximately 4.3× that of the P3SN at $z < 18$, although we note that the Population III SFRD nearly reaches the fiducial level at $z = 9$. The P3SN simulation demonstrates how feedback and the IMF are intimately linked, making high-redshift predictions of Population III stellar populations difficult without further observational data.

Considering the P3SN run, we also note that the classical Population III rate falls to zero during several cosmic epochs: $z = 18 \rightarrow 16$, $14 \rightarrow 12.5$, $12 \rightarrow 11$, and $10 \rightarrow 9$. This is due to the increased metal generation coupled with the instantaneous mixing assumption that is typically used in simulation cells polluted with SN ejecta. Our subgrid model exhibits continued Population III star formation in regions of unpolluted gas during these intervals, again pointing to the improvement in accuracy gained by modeling the mixing time at subgrid scales.

As pointed out in Paper II, the increase in star formation immediately before reionization, $z_{\rm re} \approx 8.5$, correlates strongly with an even larger relative increase in the Population III star formation rate. This is caused by a significant number of new halos crossing the star formation density threshold immediately before reionization increases the temperature of the gas (Furlanetto & Oh 2008). Reionization is essentially an instantaneous event in the simulation. Post-reionization the mass threshold for Population III star formation in new halos is increased because of the increase in the gas temperature. Since Population II star formation takes place in more massive galaxies, overall star formation continues at the previous rate, while Population III star formation drops rapidly. Hence, we predict that the largest number of galaxies dominated by Population III stars—and Population III flux—will be found just prior to reionization.

The top panel of Figure 2 supports this conclusion and depicts the fraction of halos that have at least 90% of their stellar mass in Population III stars—henceforth "Population III dominated" galaxies—as a function of redshift. The increase in the number of new Population III dominated galaxies is clearly visible at $z = 9$. The bottom panel depicts a histogram of Population III dominated galaxies binned in mass, for the fid run, and clearly shows that Population III dominated halos also attain their highest masses during the pre-reionization epoch.

The top panel in the figure also indicates that ≈25% of galaxies are Population III dominated, at $z = 9$, except in the

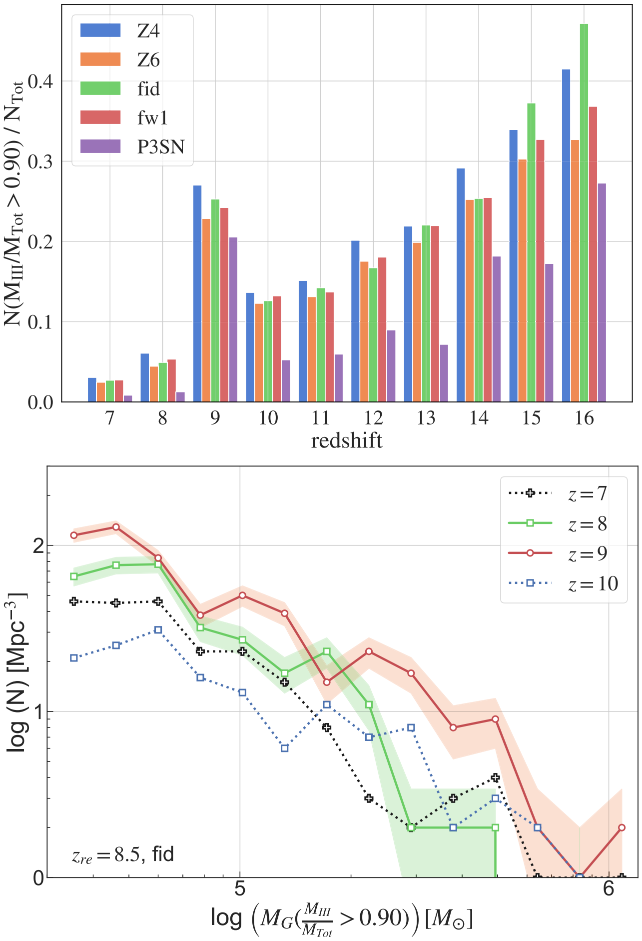

**Figure 2.** Top: the fraction of Population III dominated galaxies (defined as galaxies with at least 90% of their stellar mass in Population III stars) across all runs sharply increases immediately before reionization at $z = 9$. Considering all of the runs except P3SN, fully 25% of galaxies, pre-reionization, are Population III dominated, while only 5% are post-reionization. Bottom: the histogram depicts counts per comoving Mpc$^3$ for Population III dominated galaxies, binned by galaxy stellar mass. The plot also indicates that galaxies attain their peak masses, for the fid run, at $z = 9$ (red) vs. post-reionization (green). The shaded regions indicate $1\sigma$ Poisson errors.

P3SN case. However, by $z = 8$ the majority of star formation is taking place in preexisting polluted galaxies, and the fraction of Population III dominated galaxies drops to ≈5%. While the P3SN run generates the lowest fraction of Population III stars, the difference between the number of Population III dominated galaxies pre- and post-reionization is just as dramatic. At $z = 9$, ≈21% of galaxies are Population III dominated. This falls to slightly more than 1% by $z = 8$, again a 20% drop as exemplified by the other runs.

While the overall fraction of Population III dominated galaxies is greater at $z > 13$ than at $z = 9$, as we discuss in the next section, the fraction of potentially observable galaxies falls off quickly at $z > 10$ for all of our models.

Figure 3 depicts the metallicity of the gas for the fiducial run at two redshifts, before and after reionization, along with galaxy locations for Population III dominated galaxies. At $z = 9$, the majority of Population III dominated galaxies are found in unpolluted regions away from existing galaxies. At $z = 8$, Population III star formation has dropped by a factor of ≈5 since reionization has raised the halo mass required to initiate star formation (Couchman & Rees 1986; Simpson et al. 2013; Bose et al. 2018). Hence, Population III star formation occurs mostly in unmixed regions within and on the edges of more massive galaxies.

### 3.1. Galaxy Luminosity

Next, we evaluate the effect of our parameters on galaxy flux. We note that relatively small changes in the fraction of Population III stars with ages <3.5 Myr can make a significant change to a galaxy's luminosity.

As noted in Section 2.6, we used a Salpeter IMF to map SP mass to stars when generating the SED for Population III and Population II SPs for runs fid, fw1, Z4, and Z6. Run P3SN used the lognormal IMF SED to model Population III SP fluxes, with $\eta_{\rm SN,III} = 0.99$, and the Salpeter IMF SED for Population II SPs, with $\eta_{\rm SN} = 0.10$. The fid_orig run used a lognormal IMF SED to model all Population III stars even though a Salpeter IMF was assumed in RAMSES for the SN mass fraction.

Figure 4 depicts LFs for two representative simulations across the redshift range $7 \leqslant z \leqslant 15$. Runs Z4, Z6, and fw1 produced LFs nearly identical to fid. The shaded areas indicate the two intrinsic magnitude limits *JWST* is expected to be able to detect in the deep campaign, $m_{\rm UV} = 31.4$ mag, and via lensing, $m_{\rm UV} = 33$ mag (Gardner et al. 2006).

The two runs produce essentially indistinguishable LFs when considering $1\sigma$ estimated errors based on Poisson noise and sample variance. Even the run P3SN, which generates ≈10× the SN feedback as compared to the other runs, displays only a small change in galaxy luminosities across the redshift and magnitude range depicted. However, the combination of feedback and the reduced number of surviving Population III stars for run P3SN does slightly reduce the brightness of galaxies.

For comparison, we include LFs by Mason et al. (2015) and O'Shea et al. (2015). The former work uses a semianalytic framework to model the UV LF based on the star formation history in DM halos. While our LF is slightly higher at $z = 9$, we are in good agreement with their model at $z \geqslant 10$.

The work by O'Shea et al. (2015) is based on the Renaissance simulations. At $z \geqslant 12$, where comparisons are available, we underperform their simulation. However, we note that the best resolution of the Renaissance simulations is 19 pc as compared to our 64.5 pc, which allows them to capture star formation earlier, in smaller halos.

The consistency of these results across simulations indicates that our predictions for the luminosity of high-redshift galaxies in Paper II are robust across this parameter space. While we have yet to look at the effects of self-consistently treating reionization, it is promising to note that the luminosity of these galaxies does not seem to be highly correlated with the critical metallicity, SN loading, or the additional energy generated by a top-heavy Population III IMF.

### 3.2. Population III Flux

While our parameter variations do not result in striking changes to the LFs of our high-redshift galaxies, they do produce changes in the fraction of Population III flux coming from them. Here we briefly discuss galaxies with a Population III flux fraction down to $10^{-3}$ but focus on "observable Population III-bright galaxies" that have $m_{\rm UV} \leqslant 31.4$ mag and $f_{\rm III}/f_{\rm Tot} \geqslant 0.75$. These galaxies are important to future observational searches for Population III stars.

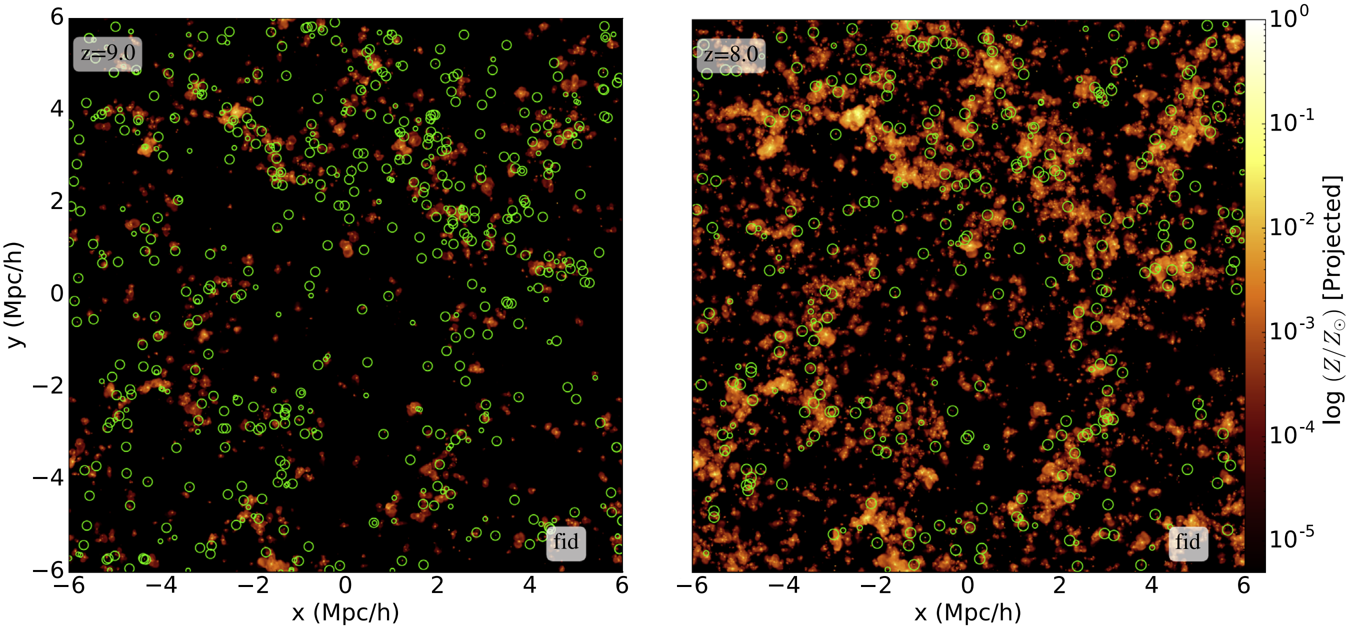

**Figure 3.** Projected metallicity of the gas for the fid run at $z = 9$ (left) and 8 (right). Circles indicate Population III dominated galaxies: galaxies with $\geqslant$90% of their mass in Population III stars. Circle size indicates the relative mass of each galaxy. At $z = 9$, 25% of galaxies are Population III dominated, and most form in pristine gas away from existing galaxies. By $z = 8$, Population III star formation in new halos is mostly quenched since reionization raises the gas temperature and therefore the halo mass required to initiate star formation. At this redshift 5% of galaxies are Population III dominated. Scale is comoving Mpc $h^{-1}$.

Figure 5 depicts the Population III flux fraction for runs fid and P3SN that display the greatest difference across redshifts. We have normalized the probabilities in each magnitude bin such that they sum to 1, making it easy to see the distribution of Population III flux per magnitude bin. For the fid run, Population III flux from hybrid galaxies, $10^{-3} < f_{\rm III}/f_{\rm Tot} < 0.5$, is dominant since Population III stars are assumed to be lower mass and hence long-lived. For P3SN this pattern is inverted: we note a dearth of hybrid galaxies since massive Population III stars from the lognormal IMF live short but radiatively intense lives. This results in relatively little Population III flux except for the small fraction of galaxies in which these massive stars are shining. Here, they dominate the flux of the galaxy (top row of bins). However, once they are gone, the Population III flux quickly falls below $f_{\rm III}/f_{\rm Tot} \leqslant 10^{-3}$. This bimodality is most evident before reionization, when new halos form Population III stars from the pristine gas. Once they die, the galaxy is dominated by Population II flux. However, most of the Population III-bright galaxies at $z \geqslant 9$ are on the edge of visibility for giant telescopes like *JWST*. At lower redshift, $z < 9$, the vast majority of galaxies have only a tiny fraction of Population III flux: $f_{\rm III}/f_{\rm Tot} \approx 10^{-3}$, in agreement with the lack of current observations of Population III-bright galaxies.

The second factor contributing to the bimodal flux distribution in run P3SN is the 10-fold increase in SN energy. SNe in P3SN efficiently evacuate the gas from the host halo, contributing to the reduction in the number density of hybrid galaxies. Considering the typical (also the minimum) SP mass, $M_\star \geqslant 8.3 \times 10^3\ M_\odot$, we find that the SN energy generated by Population III SNe is at least $8.2 \times 10^{53}$ erg. The top panel of Figure 6 depicts the range of halo DM masses in this simulation, as a pdf, while the bottom panel plots the estimated gravitational binding energy (Loeb 2010),

$$E_{\rm b} = 2.9 \times 10^{53}\left(\frac{M_{\rm h}}{10^8\ M_\odot}\right)^{5/3}\left(\frac{1+z}{10}\right){\rm erg}, \qquad (7)$$

for these halos. When considering an SN-to-gas coupling efficiency of 10% (Kitayama & Yoshida 2005; Whalen et al. 2008; Hartwig et al. 2018), we note that Population III SNe efficiently evacuate the gas from median mass halos and below, which have binding energies $\lesssim 4.3 \times 10^{52}$ erg.

Our stellar and SN feedback models are not directly comparable to those described in the above references.[7] However, our purely mechanical SN feedback acts on SN ejecta mass on the order of the SP mass for our P3SN simulation. This level of parameterized coupling effectively helps to evacuate gas and quench star formation in SN-hosting cells.

Population III-bright galaxies, as a fraction of all observable galaxies, are summarized in Figure 7. Since the fractions of Population III-bright galaxies for runs fw1, Z4, and Z6 are very similar to the fid run, here we only include a comparison between fid and P3SN. For a comparison between fid and fid_orig see the Appendix. We use the *JWST* limiting magnitude of $m_{\rm UV} = 31.4$ mag, along with a lensing magnitude limit of $m_{\rm UV} = 33$ mag, to identify observable galaxies with at least 75% of their flux coming from Population III stars.

For run P3SN the fraction of observable Population III-bright galaxies is 33% at $z = 12$. However, there are only three galaxies with $m_{\rm UV} \leqslant 31.4$ mag at this redshift, and hence the uncertainty is very large. The statistics are similarly weak at $z = 10$, where we find a single Population III-bright galaxy out of 27 observable galaxies (4%). Hence, we note that, as in our previous work, the largest statistically significant fraction, ≈19%, of observable Population III-bright galaxies occurs immediately before reionization. Again, this is due to new

---

[7] Hartwig et al. (2018) modeled a coupling efficiency of 10% between the SN energy and the surrounding gas. Our simulations assumed that 10× the mass ejected by SNe is swept up and carried out of the cell.

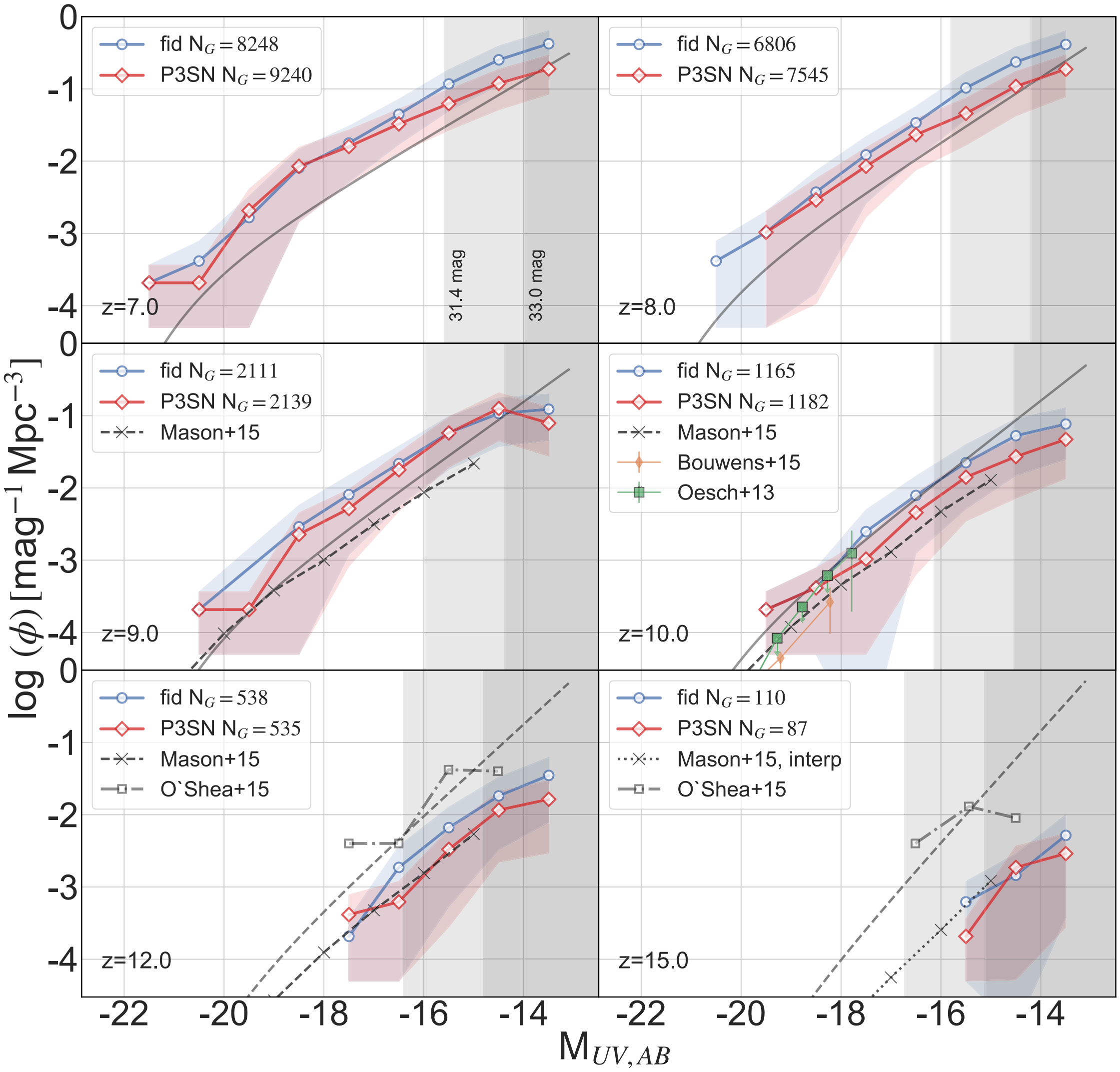

**Figure 4.** UV LFs derived from our P3SN and fid simulations with $1\sigma$ error bounds including both Poisson noise and sample variance. Magnitude bins are labeled at their right edge. Solid gray lines are Finkelstein (2016) Schechter fits. Dashed gray lines are extrapolated. The largest variation between simulations for the parameters studied is between these runs. P3SN exemplifies a slight drop in the luminosity at the faint end at most redshifts due to the increased SN feedback that helps to quench star formation in less massive halos coupled with an IMF with far fewer long-lived, low-mass stars. For $z = 10$, we have included Bouwens et al. (2015) and Oesch et al. (2013) observational data, with errors. We also include LFs derived from models and simulations by Mason et al. (2015) and O'Shea et al. (2015). We note that for $z = 15$ we interpolated the Mason et al. (2015) data that were available for $z = 14$ and $z = 16$. The shaded areas of the plots indicate likely limiting intrinsic magnitudes for *JWST* ultradeep and lensed observations.

halos crossing the density threshold for star formation before the UV background raises the temperature of the gas.

As shown when discussing Figure 5, none of our galaxies were Population III-bright at the $m_{\rm UV} = 31.4$ mag limit for the fid run. To detect galaxies with a significant fraction of Population III flux, we have to go to $m_{\rm UV} = 33$ mag, where, once again, the largest statistically significant fraction of Population III-bright galaxies occurs at $z = 9$. The flux from the fid run's Salpeter IMF of longer-lived, low-mass stars simply does not outshine the few, short-lived massive stars modeled by the lognormal IMF in run P3SN.

Once again, reionization in our simulation is essentially an instantaneous event. In reality, it was a patchy, extended process, and hence our result does not map universally onto any observed field where sample variance is a factor.

The greatest effect on predicted counts of Population III-bright galaxies occurs when we consider a *JWST* lensing limit of $m_{\rm UV} \leqslant 33$ mag and run P3SN. At $z = 10$ and 11 we predict that $\approx$15% of Population III-bright galaxies will have an intrinsic magnitude such that 10× lensing magnification will make them observable by the *JWST*. At $z = 12$, run P3SN has approximately the same fraction of $m_{\rm UV} \leqslant 33$ mag Population III-bright galaxies as at $m_{\rm UV} \leqslant 31.4$ mag, but the Poisson uncertainty for the former is far lower. While the $z = 13$ and 14 statistics also indicate significant fractions of Population III-bright galaxies at $m_{\rm UV} \leqslant 33$ mag, the $1\sigma$ uncertainties are large. However, even considering the worst case, more than 5% of Population III-bright galaxies at $z = 13$ have $m_{\rm UV} \leqslant 33$ mag. Hence, lensing campaigns should provide *JWST* with opportunities to observe Population III galaxies beyond $z = 10$, but once again the redshift immediately before reionization contains the largest fraction of Population III-bright galaxies when considering Poisson statistics.

### 3.3. Chemical Composition

Using $\overline{Z_{{\rm P},\star}}$, $\overline{Z_\star}$, and $P_\star$, we model the fraction of stellar mass in each SP that represents Population III stars, as well as

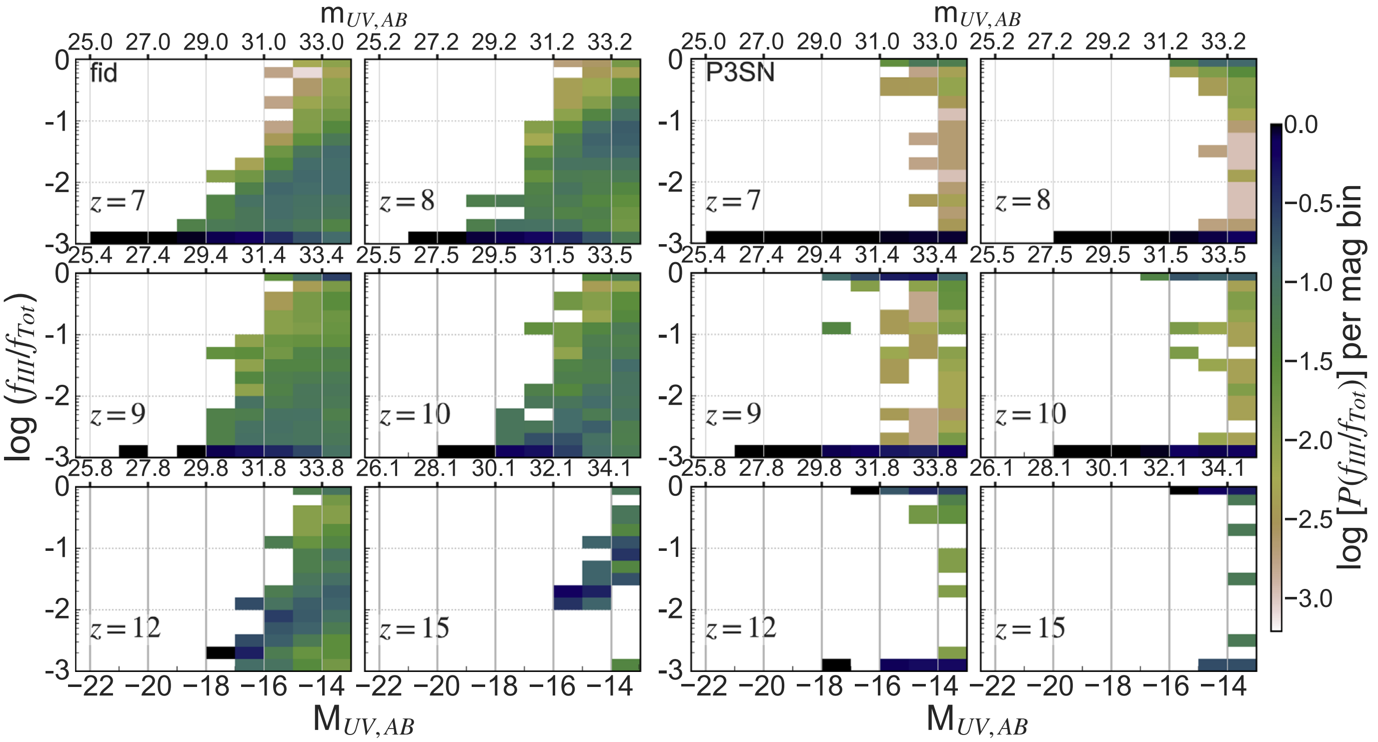

**Figure 5.** Normalized probability, per magnitude bin, for the rest-frame UV Population III flux fraction, $f_{\rm III}/f_{\rm Tot}$, for our galaxies. Magnitude bins are labeled at their right edge. The top row of bins represents $f_{\rm III}/f_{\rm Tot} \geqslant 75\%$; the next row, 50%. Left: fid run that used a Salpeter IMF for all SPs. Here, Population III stars are low mass and longer-lived, giving rise to hybrid galaxies with small fractions of Population III flux. Right: run P3SN. Here the probabilities of finding hybrid galaxies with $10^{-3} < f_{\rm III}/f_{\rm Tot} < 0.5$ decrease drastically. This is due to the increased feedback in the P3SN simulation combined with the lack of older Population III stars. However, the fraction of Population III-bright galaxies (top row of bins) is greater than fid at all redshifts since Population III star formation in new halos that follows the lognormal IMF results in very luminous high-mass stars. While the fraction of galaxies with $f_{\rm III}/f_{\rm Tot} \geqslant 0.75$ is significant at $z \geqslant 9$, the vast majority of galaxies are beyond the magnitude limits for unlensed *JWST* observations. See Figure 7, which summarizes the data for Population III-bright galaxies.

the enhanced metallicity of the polluted fraction of Population II stars, $Z_\star = \overline{Z_\star}/(1 - P_\star)$, as described in Section 2.3.2. To simplify direct comparisons with our earlier work, we once again, for our initial analysis, adopt the elemental abundance pattern generated by a 60 $M_\odot$ Population III SN (Heger 2018) as representative of metal yields in the 20 $M_\odot \leqslant M_\star < 120\,M_\odot$ range, the dominant region of our Population III IMF that produces carbon-enhanced material. Specifically, the abundances of each element in each SP are computed by mapping the mass fraction of primordial metals, $Z_{{\rm P},\star}$, to the abundances found in this ejecta. "Regular metals," which have a mass fraction $Z_\star - Z_{{\rm P},\star}$, are modeled using abundances provided by F. X. Timmes (2016, private communication) and are representative of typical Type II SN abundances. Details are discussed in Paper I.

Note that the primordial metals, $Z_{{\rm P},\star}$, were generated by the mass fraction of each Population III SP that underwent an SN after 10 Myr. These are stars $\gtrsim 16\,M_\odot$ in each IMF. This corresponds to 99% of the mass of each SP for our lognormal IMF but only 10% of the SP mass for the Salpeter IMF.

Using the criteria from Beers & Christlieb (2005), we identified the mass fractions of our Population II SPs that are ultra−metal-poor (UMP, [Fe/H] $< -4.0$) and carbon-enhanced ([C/Fe] $> +0.7$). Our fraction of such stars for runs fid, Z4, Z6, and P3SN is in very good agreement with observations for this class of star in the MW halo (see Yoon et al. 2018, Figure 6). Comparisons to the fraction of observed CEMP-no stars at metallicities greater than UMP diverge, with the simulations underperforming observations, since stars with [Fe/H] $> -4.0$ are still being formed in the simulation at $z \geqslant 7$.

Moving on to a more detailed chemical analysis, Figure 8 depicts the mass-weighted pdf's for the chemical abundance of [C/H] as a function of metallicity for the fid and P3SN simulations' SPs. Results for runs Z4, Z6, and fw1 are very similar to the fid run. We focus on carbon since it characterizes CEMP-no stars (Beers & Christlieb 2005). The observed chemical composition of CEMP-no stars in the MW halo requires SN progenitors from a top-heavy IMF with stars that end their lives as Type II SNe, leaving a BH or neutron star that traps the heavier elements. Several stars in the mass range of our lognormal IMF result in SNe with such carbon-enhanced yields (Heger & Woosley 2002).

Each plot is overlaid with the set of CEMP-no stars from Yoon et al. (2016) and includes a dashed line depicting a reference [C/Fe] ratio of 0.7. While both plots depict an enhanced probability of finding stars with [C/Fe] $\approx 0.5$, the P3SN data more clearly display the bimodal relationship between carbon and iron discussed by Yoon et al. (2016). This plot depicts the enhanced probability of finding stars with $0 <$ [C/Fe] $\lesssim 1$, likely indicative of a population of CEMP-no stars polluted by both Population III and Population II SNe, as well as a population of very metal-poor stars with [Fe/H] $< -2$ and [C/H] $\approx -1$, a population likely polluted solely by Population III SNe.

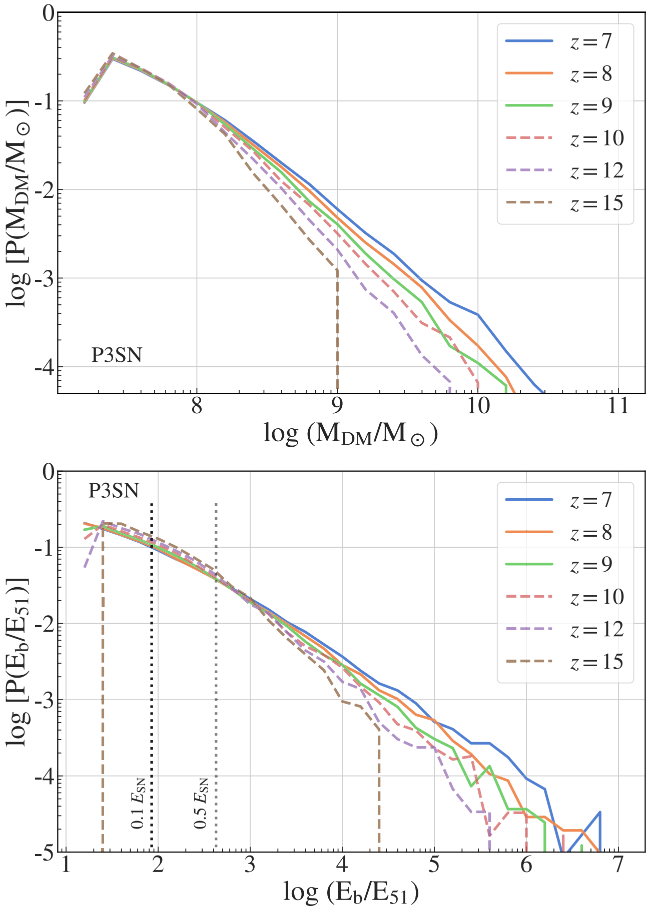

**Figure 6.** Top: halo DM mass function (HMF) for P3SN expressed as a normalized pdf. As expected, the HMF indicates that the majority of galaxies have $M_{\rm DM} < 10^8\,M_\odot$ at all redshifts. Bottom: gravitational binding energy (in units of $10^{51}$ erg) for P3SN galaxies expressed as a normalized pdf. The dotted line labeled "0.1 $E_{\rm SN}$" indicates a conservative fraction of SN energy (10%) that couples to the gas when considering the minimum SP mass. Galaxies with binding energies below this threshold should lose their baryons as a result of a single P3SN Population III SP SN. This includes galaxies up to the median binding energy. An average of 67%, by number, of halos become unbound by P3SN SNe, across redshifts. We include a higher coupling efficiency factor of 0.5 $E_{\rm SN}$, for reference.

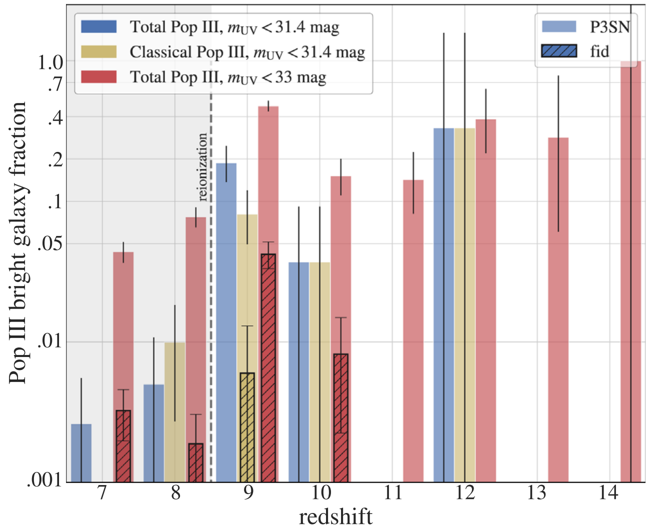

**Figure 7.** Comparison of the fraction of Population III-bright galaxies for the P3SN and fid runs, with Poisson error bars. The plot depicts the probability, per redshift, of finding an observable, $m_{\rm UV} \leqslant 31.4$ mag (blue) or $m_{\rm UV} \leqslant 33$ mag (red), Population III-bright, $f_{\rm III}/f_{\rm Tot} \geqslant 0.75$, galaxy as a fraction of all galaxies meeting the magnitude cutoff. We include yellow bars that consider only classical Population III star formation for comparison. For P3SN, 19% of observable galaxies at $z = 9$ are Population III-bright. At $z = 12$, 33% are Population III-bright galaxies, but there are only three galaxies with $m_{\rm UV} \leqslant 31.4$ mag, resulting in a large uncertainty. We conclude that the best epoch in which to look for observable Population III-bright galaxies is immediately before reionization.

We also model Population III SN ejecta integrated over a variety of subranges of our P3SN IMF using the yields from Heger & Woosley (2010) and Nomoto et al. (2013) making use of the SYGMA (Ritter et al. 2018a, 2018b) software library.

Figure 9 depicts the results of this analysis. We only include plots for a representative subset of the runs using Population III SN yields from Heger & Woosley (2010). The yields from Nomoto et al. (2013) include the iron-rich ejecta from pair-instability SNe (progenitors from 140 to 300 $M_\odot$) and result in subsequent generations of stars with [C/Fe] ≈ 0. Even restricting the Nomoto et al. (2013) yields to a maximum progenitor of 120 $M_\odot$, we find that the resulting range of [C/Fe] in our Population II stars does not match the range of CEMP-no observations or the yields generated by Heger & Woosley (2010).

The top left panel of Figure 9 covers the mass range from 10 to 120 $M_\odot$, near the top of the range in which heavier elements are trapped in a compact remnant. While Population III stars with $M \lesssim 16\,M_\odot$ likely live longer than the 10 Myr assumed for Population III SNe, we include their yields in the subplot to demonstrate the effect these lower-mass stars have on the [C/Fe] distribution.

Adjusting the low-end mass of the IMF to 20 $M_\odot$ (top right panel) results in a better match to the observed chemical abundances of CEMP-no stars since the amount of iron in SN ejecta from 10 $M_\odot$ progenitors lowers the maximum [C/Fe] ratio substantially. Assuming a higher characteristic mass of 120 $M_\odot$ (bottom right panel) results in the best match when integrating SN yields across an IMF. However, as can be seen in the bottom left panel, the value of the characteristic mass does not have a large effect on the probability distribution. Changing the characteristic mass from 20 to 120 $M_\odot$ changes the maximum [C/Fe] ratio by 0.67 dex. However, changing the bottom of the IMF range from 10 to 20 $M_\odot$ results in an increase in the [C/Fe] ratio of ≈2.1 dex, or a factor of ≈138. Lastly, we note that the overall peak carbon abundances, relative to solar, are lower when integrating an IMF of SN yields as compared to the single progenitor model depicted in Figure 8.

This analysis argues for an IMF biased toward stars with a large characteristic mass and a steep drop in the fraction of stars below 20 $M_\odot$—one that is greater than that modeled by a lognormal IMF. Devising and modeling such IMFs could be tackled in a follow-on project. Of course, these results are very sensitive to the adopted set of Population III yields, and these are still highly uncertain. We also note that not all halos would generate stars across the entire mass range. If the first minihalos generated small clusters of stars, a stochastically sampled IMF would better model the resulting chemical enrichment.

Even so, this agreement between the P3SN simulation and observations further supports the idea of a top-heavy IMF. It

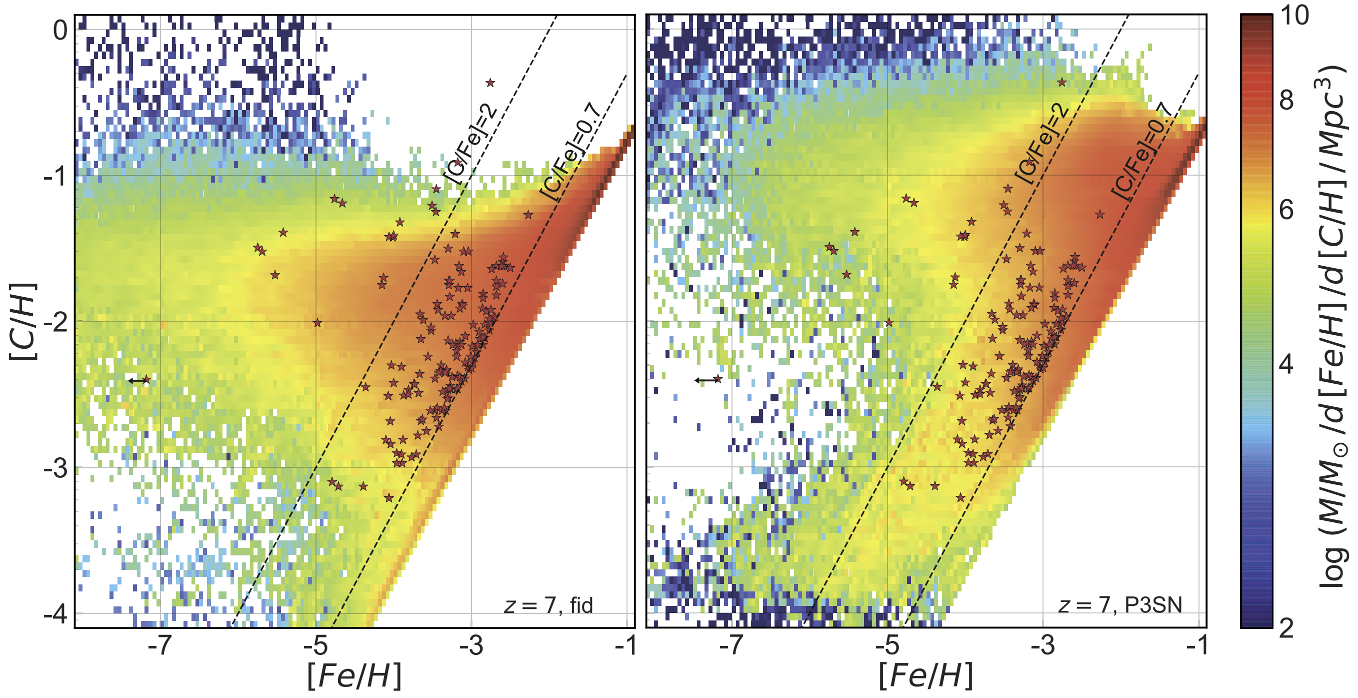

**Figure 8.** Joint pdf's depicting the mass-weighted probabilities for the chemical abundance of [C/H] as a function of [Fe/H] for all SPs in our fiducial (left) and P3SN (right) simulations at $z = 7$. Carbon levels are higher in the P3SN simulation owing to the larger fraction of carbon-rich Population III SN ejecta generated by the top-heavy IMF. It is the best match to observations of CEMP-no stars (red stars; Yoon et al. 2016). The P3SN plot also depicts an enhanced probability of finding stars with $0 < [\mathrm{C/Fe}] \lesssim 1$, as well as a population of more metal-poor stars with $[\mathrm{Fe/H}] < -2$ and $[\mathrm{C/H}] \approx -1$. The dashed lines indicate $[\mathrm{C/Fe}] = 0.7$ and $[\mathrm{C/Fe}] = 2.0$.

ties the nucleosynthetic products of Population III SNe to the chemical composition of ancient MW CEMP-no halo stars.

## 4. Conclusions

We have conducted a parameter study analyzing the results of five large-scale cosmological simulations to assess the observational consequences of some of the unknown properties related to Population III star formation. In particular, our simulations have explored the effects of

1. lowering the SN mass-loading factor, that describes the amount of circumstellar gas carried along with SN ejecta, from 10 times the ejecta mass to 1;
2. varying the value of the critical metallicity that marks the boundary between Population III and Population II star formation between $10^{-6}$ and $10^{-4} Z_{\odot}$; and
3. implementing a lognormal Population III IMF in place of the Salpeter IMF, resulting in an ≈10-fold increase in both the amount of SN energy and metals injected into the ISM.

We have compared these simulations to each other and to the run from Paper II, fid_orig, quantifying the differences and analyzing the implications for predictions made in our previous work.

We find that the parameter range explored does not produce a large spread in the overall SFRD. The largest change, produced by P3SN, results in approximately a 50% reduction in the total SFRD at $z \leqslant 12$ and less at $z \leqslant 9$. The differences between the fid and P3SN run are within sample variance at $z \leqslant 12$. Looking at the Population III SFRD, run P3SN again produces the largest change from the fiducial case, this time significant, resulting in a decrease of an average of approximately 0.64 dex (a factor of $\approx 1/4$) averaged over the redshift range $7 \leqslant z < 18$. This points to the importance of understanding the Population III IMF since it has a direct impact on the fraction of surviving Population III stars at every epoch. Additionally, understanding the IMF relates directly to the amount of SN feedback. The amount of SN feedback is important since it is relatively easy to evacuate the gas from low-mass halos in the early universe.

However, once again we see that modeling the pristine fraction of gas has a significant effect on the Population III SFRD. The subgrid model produces a Population III SFRD a factor of 2 above the classical model for all simulations except P3SN. For P3SN the difference between the classical Population III SFRD and the subgrid model was even more pronounced, with the classical rate falling to zero during several epochs. We did not see an appreciable difference when varying the critical metallicity for Population III star formation over 2 orders of magnitude. This reinforces our conclusion that even at a physical resolution of 64.5 pc, modeling the subgrid evolution of the pristine fraction of gas is more important than knowing the value of the critical metallicity.

We find that Population III star formation peaks immediately before reionization, in all of our simulations. This is true in terms of both the mass of Population III dominated galaxies and their number counts. This result is consistent with our previous work and reinforces our conclusion that this is the best epoch in which to search for Population III stars.

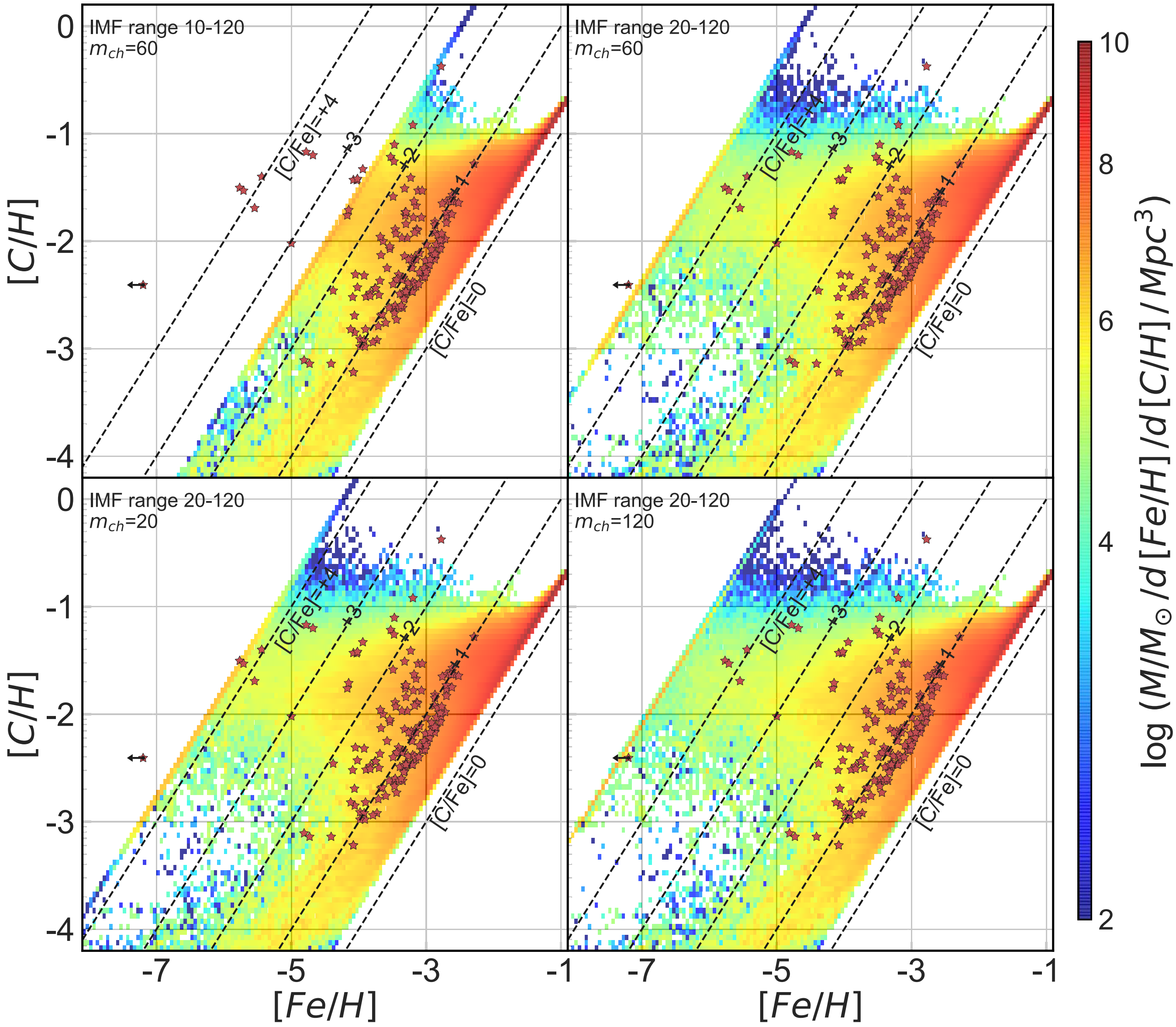

**Figure 9.** Same as Figure 8, but for an integrated IMF of yields over the range specified in each panel. All data based on run P3SN at $z = 7$ and yields from Heger & Woosley (2010). The characteristic mass was also varied as indicated. Comparing the panels, we note that adjusting the floor of the mass range has a larger effect on the final ratio of [C/Fe] than the characteristic mass. Once again, observations are from Yoon et al. (2016).

While observational constraints on the high-redshift LF are uncertain (Bouwens et al. 2015; McLeod et al. 2015; Oesch et al. 2015; Finkelstein 2016), we find that our model predictions approximately follow the predicted faint-end slope at $8 \leqslant z \leqslant 10$ and are in reasonable agreement with extrapolated Schechter functions to $z = 12$. We suspect that our simulations' resolution and relatively small volume limit our ability to accurately model galaxy counts at $z = 15$, as they underperform both extrapolated Schechter models and O'Shea et al. (2015) but are in reasonable agreement with LFs based on analytic models of star formation in high-redshift DM halos by Mason et al. (2015). None of our simulated galaxies are brighter than $m_{\rm UV} = 31.4$ mag at $z > 13$.

We note that the largest differences in Population III-bright galaxies, with at least 75% of their flux coming from Population III stars, occur between the fiducial and P3SN simulations. The feedback effects of the Population III lognormal IMF coupled with the small number of Population III stars that survive beyond 10 Myr result in far fewer galaxies with moderate Population III flux fractions between 0.75 and $10^{-3}$. The added feedback quenches subsequent star formation in median-sized galaxies and below, resulting in a largely bimodal "all-or-nothing" distribution of Population III flux fractions for P3SN galaxies. These galaxies vary between purely young, small Population III galaxies and older, larger Population II dominated galaxies that possess a tiny fraction of older, low-mass Population III stars.

When considering the fraction of observable Population III-bright galaxies, most of the simulations produce statistics very similar to the fid run. This run predicts no Population III-bright galaxies across the redshift range studied. However, the P3SN model stands out. While the fraction of Population III-bright galaxies with $m_{\rm UV} \leqslant 31.4$ mag is less than 1% post-reionization, the fraction increases to approximately 19% immediately before reionization. Additionally, the number of lensing opportunities for galaxies with $m_{\rm UV} \leqslant 33$ mag for the P3SN run is encouraging at $z > 9$, where we predict their occurrence at more than 1 in 10, although with weak statistics at $z > 12$.

Turning to the chemical composition of our stars, we demonstrated that our P3SN simulation, with a lognormal IMF for metal-free stars with a characteristic mass of 60 $M_\odot$, results in subsequent generations of stars with elemental abundances that reproduce the two populations of CEMP-no stars observed in the MW halo. In particular, our model reproduces the bimodal distribution of these stars, where we see one population of CEMP-no stars likely polluted solely by Population III SNe with $[{\rm C/H}] \approx -1$ and a second population likely polluted by both Population III and Population II SNe with a higher overall metallicity and $[{\rm C/Fe}] \approx +0.7$. This supports the notion of a Population III IMF characterized by stars in the $20\, M_\odot \leqslant M_\star < 140\, M_\odot$ range.

We also integrated SN yields across subranges of our lognormal IMF. We found that stars in the 20–120 $M_\odot$ mass range result in a subsequent generation of polluted stars that correlate well with observations of CEMP-no MW halo stars. Once again, this supports the assumption that early minihalos generated a few Population III stars with masses predominately in this range but possibly biased even more toward the heavier end of this range than predicted by a lognormal distribution. Of course, there are still large uncertainties in the nucleosynthetic products of Population III SNe.

Including stars more massive than 140 $M_\odot$ in our IMF yields resulted in $[{\rm C/Fe}] \approx 0$ and a subsequent generation of Population II stars that did not match observations. This result is at least in part due to the simulations' SP mass resolution. While as few as one to four Population III stars may have been created in early minihalos, our simulations' SP mass resolution of $8.6 \times 10^3\, M_\odot$ means that stars greater than 140 $M_\odot$ were represented in all star-forming galaxies. Increasing the mass resolution of our simulation would address this shortcoming.

A natural follow-on to this study would be to examine the effects of stochastically sampling the IMF across the range of masses to determine the effects of the various SN yields on the chemical composition of subsequent stellar generations. Such a study could help to further pin down the Population III IMF with regard to observations of metal-poor stars. This and subsequent studies will help to further our understanding of the Population III IMF and the physical processes relevant to modeling the evolution of high-redshift galaxies.

We would like to thank Jinmi Yoon for supplying us with data for CEMP-no stars, as well as Rogier Windhorst and Seth Cohen for fruitful discussions and suggestions. Special thanks to Alexander Heger for answering several questions about Population III SN yields.

This work was supported by the National Science Foundation under grants AST-1715876 and PHY-1430152 (the Joint Institute for Nuclear Astrophysics—Center for the Evolution of the Elements) and NASA theory grant NNX15AK82G. B.C. was also supported by the ERC Consolidator Grant (Hungary) funding scheme (project RADIOSTAR, GA no. 724560). The simulations and much of the analysis for this work were carried out using the NASA High-End Computing Capability (HECC) and the Texas Advanced Computing Center (TACC) at the University of Texas at Austin under grant TG-AST130021. We would also like to thank the NASA HECC support team.

*Software:* RAMSES (Teyssier 2010), AdaptaHop (Colombi 2013), MUSIC (Hahn & Abel 2013), pynbody (Pontzen et al. 2013), SYGMA (Ritter et al. 2018a, 2018b), yt (The yt project 2010).

## Appendix

In this appendix we briefly compare the results from fid_orig (Paper II), fid, and, for Population III-bright galaxies, the P3SN simulations. The results for fid and fid_orig are based on the same RAMSES simulation data and hence used the same SPs, at each redshift. Specifically, the surviving fraction of SP mass after 10 Myr, 90%, corresponds to a Salpeter IMF. The analysis of the fid data also assumed this distribution of mass, in post-processing, for the surviving stars when computing flux. Hence, most of the stellar mass was concentrated in smaller, long-lived stars. However, for fid_orig, we assumed a lognormal distribution of stellar mass for the surviving fraction of each SP, resulting in a much larger fraction of massive, short-lived stars. Run P3SN modeled a lognormal IMF within RAMSES, and hence 99% of each SP's mass was lost to SNe after 10 Myr. Even with this reduction in mass, the fraction of massive young stars results in flux comparable to the fid case as depicted in Figure 4.

Figure 10 compares the LFs for fid and fid_orig. As depicted, the change in the IMF used to interpret stellar mass—along with the corresponding SEDs for Population III stars —results in only very small changes to the LFs of our galaxies. It appears that the increased luminosity of the small fraction of massive, young Population III stars in the fid_orig lognormal IMF is mostly matched by the extra luminosity of the larger fraction of older Population III stars in the fid Salpeter IMF.

Figure 11 depicts the Population III flux fraction as a function of the magnitude and redshift of our galaxies for fid (left) and fid_orig (right). We have normalized the probabilities in each magnitude bin such that they sum to 1. Population III flux from hybrid galaxies, with $10^{-3} < f_{\rm III}/f_{\rm Tot} < 0.5$, in the fid run is more prominent than in the fid_orig run since the Salpeter IMF results in a larger fraction of Population III stellar mass mapped to smaller, longer-lived stars. Such stars result in moderate fractions of Population III flux. Conversely, galaxies with $f_{\rm III}/f_{\rm Tot} \geqslant 0.75$ are less populous in this model since less mass was mapped to younger, massive stars. Hence, while the IMF used in conjunction with the SEDs does not significantly affect the luminosity of our galaxies, it does make a dramatic difference in the type of flux they generate.

Figure 12 compares the fraction of Population III-bright galaxies for the P3SN and fid runs to fid_orig. We note that the fid_orig[8] run generated more, or as many, Population III-bright galaxies at $m_{\rm UV} \leqslant 31.4$ mag over the range $7 \leqslant z \leqslant 10$ than P3SN. The smaller SN fraction, 10%, in the fid_orig resulted in more mass in stars than in the P3SN run. The fid case generated no Population III-bright galaxies over this range. Additionally, the fraction of Population III-bright galaxies with $m_{\rm UV} \leqslant 33$ mag in the fid run drops by an average factor of 10 as compared to fid_orig over the same redshift range owing to the reduced fraction of mass in massive, luminous stars.

---

[8] Figure 12 presents the corrected version of fid_orig data that were plotted incorrectly in Paper II. The errors in the plot, as well as incorrect percentages mentioned in that discussion, do not affect any of our conclusions in that work.

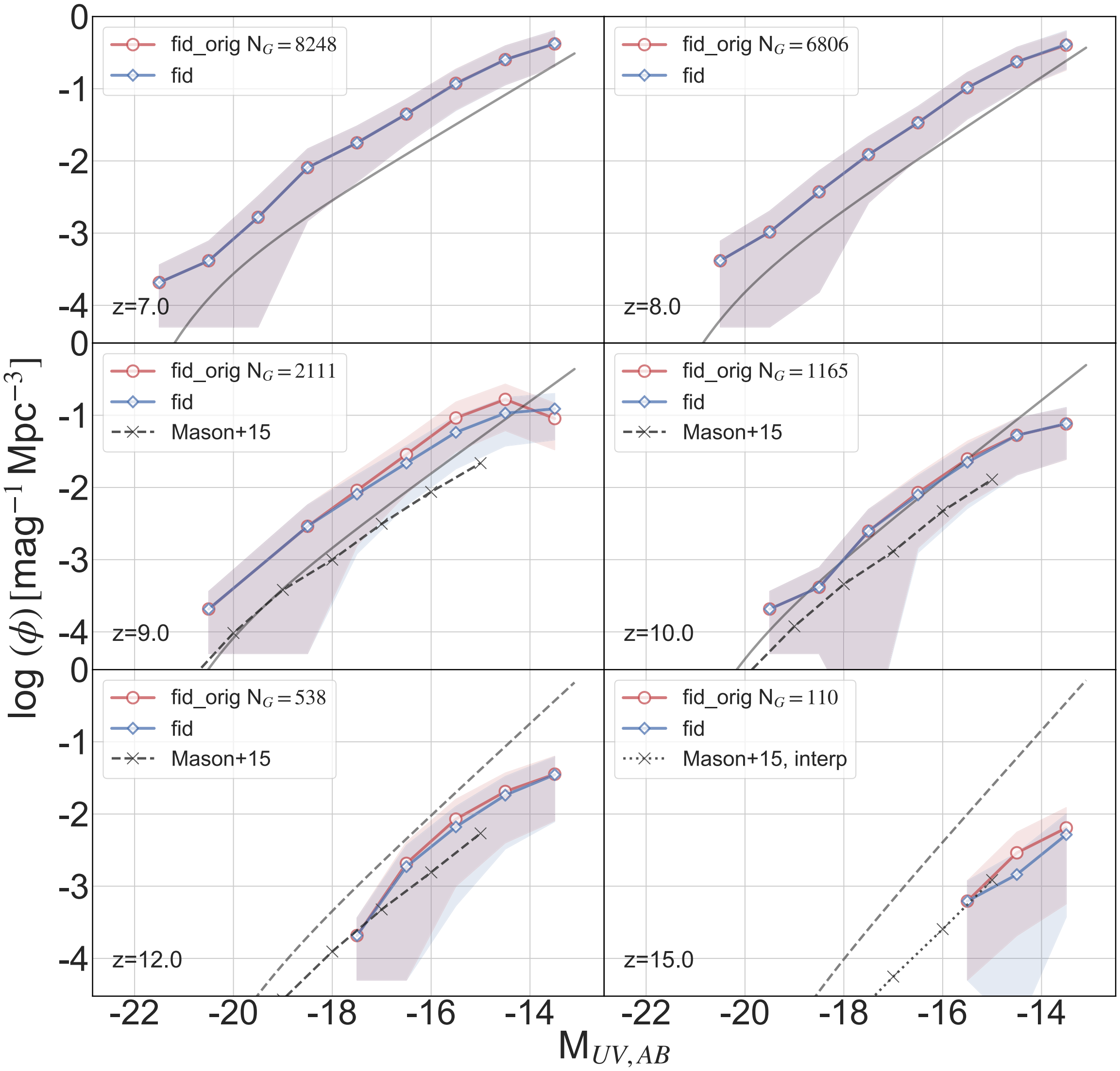

**Figure 10.** UV LFs derived from our simulations with $1\sigma$ error bounds, including both Poisson noise and sample variance. Solid gray lines are Finkelstein (2016) Schechter fits. Dashed gray lines are extrapolated. We also include LFs from Mason et al. (2015) for comparison. fid_orig uses the lognormal Population III IMF SEDs from Sarmento et al. (2018), while fid uses the Salpeter IMF SEDs. Although the interpretation of surviving SP mass is very different in these two models, the resulting overall LFs are nearly indistinguishable.

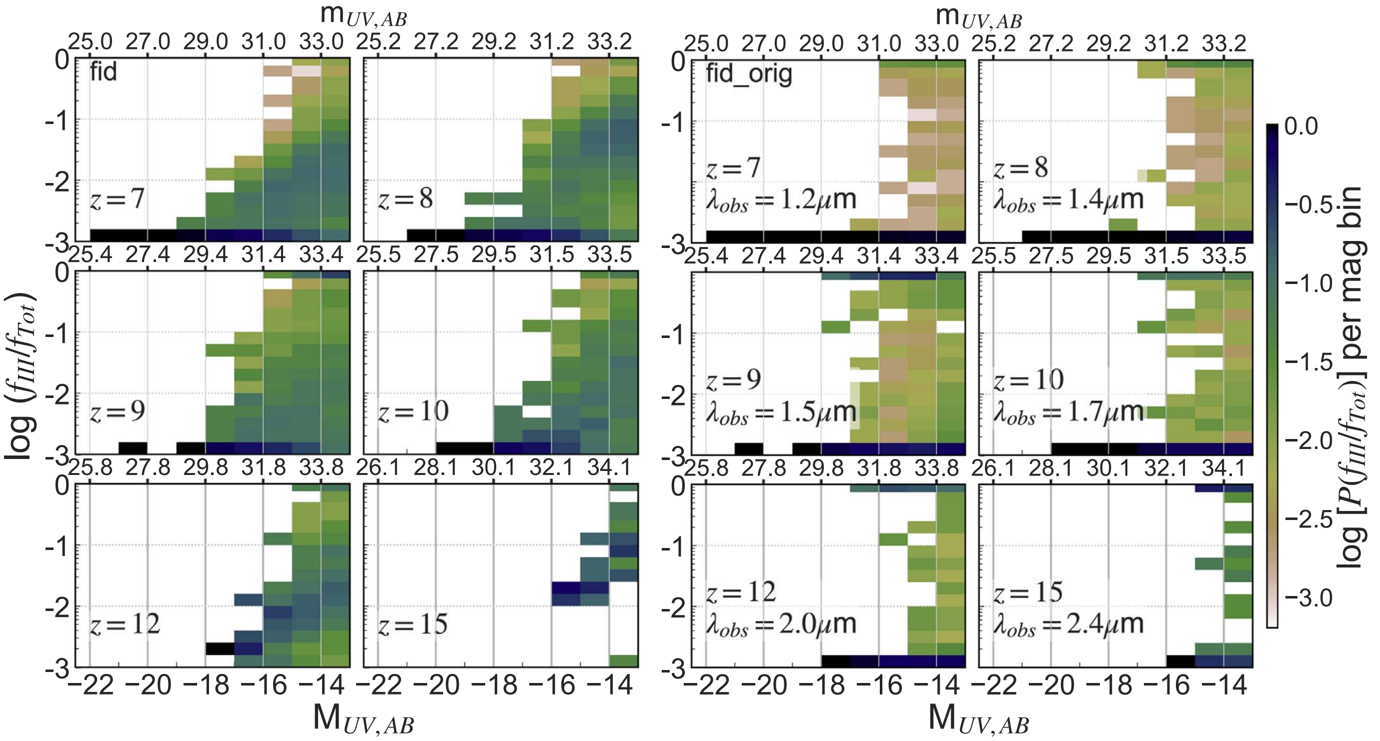

**Figure 11.** Same as Figure 5, but comparing fid (left) to fid_orig (right). The fid run modeled Population III flux derived from a Salpeter IMF. The fid_orig simulation used a lognormal IMF (Paper II) for Population III stars. SEDs based on a Salpeter IMF for Population III stars result in more flux from smaller, older stars and result in a large fraction of hybrid galaxies ($10^{-3} < f_{\rm III}/f_{\rm Tot} < 0.75$). The lognormal case, fid_orig, tends to be more bimodal, especially at $z \geqslant 10$, where ongoing Population III star formation results in a larger fraction of young, massive stars. $\lambda_{\rm obs}$ indicates the observational wavelength of the 1500 Å reference.

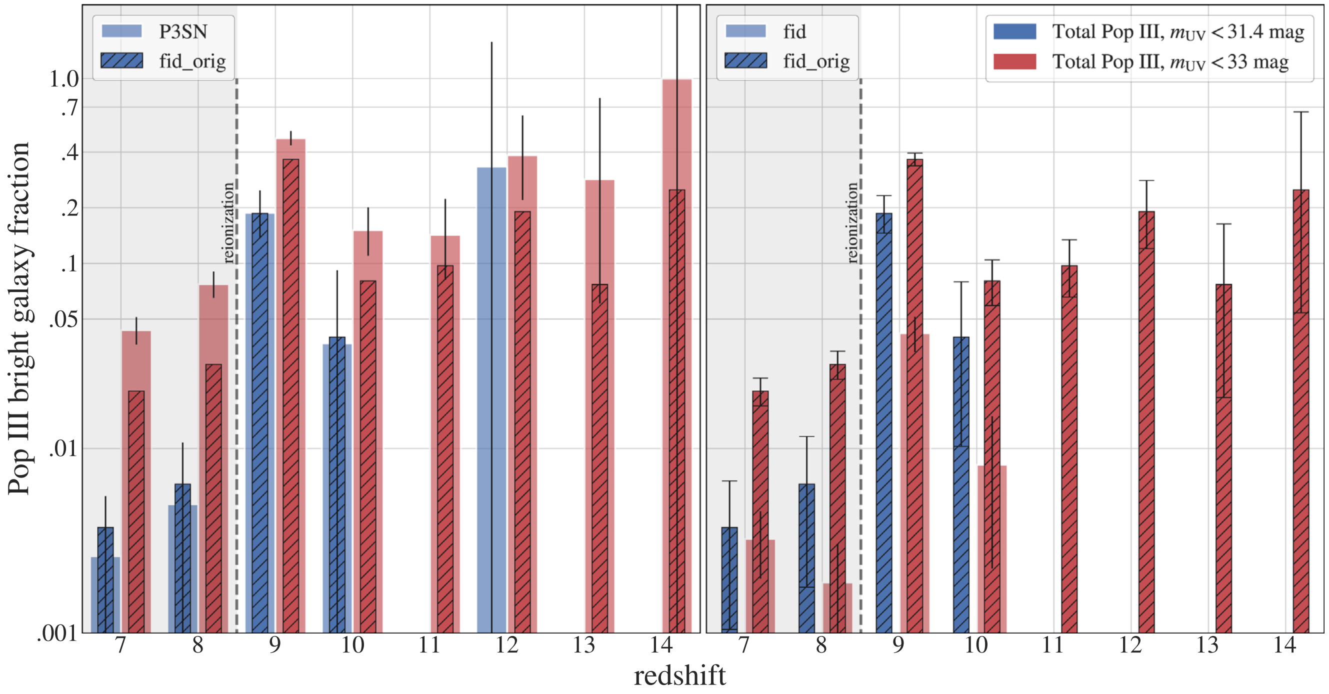

**Figure 12.** Comparison of the fraction of Population III-bright galaxies for the P3SN and fid runs to the fid_orig run, with Poisson error bars. Each panel indicates the joint probability of finding an observable, $m_{UV} \leqslant 31.4$ mag (blue) or $m_{UV} \leqslant 33$ mag (red), Population III-bright galaxy as a fraction of all galaxies meeting the magnitude cutoff. Run P3SN closely matches the fid_orig case since both of the runs model flux as coming from a lognormal distribution of stars for each SP. While fid and fid_orig have the same SP mass at each redshift, they each modeled the flux coming from the constituent stars using a different IMF: Salpeter for fid and lognormal for fid_orig. The flux from massive stars, as modeled in fid_orig, results in a much larger fraction of Population III-bright galaxies than from the stars following a Salpeter IMF in fid.

## ORCID iDs

Richard Sarmento https://orcid.org/0000-0002-8013-5970
Evan Scannapieco https://orcid.org/0000-0002-3193-1196
Benoit Côté https://orcid.org/0000-0002-9986-8816

## References

Abel, T., Bryan, G. L., & Norman, M. L. 2000, ApJ, 540, 39
Abel, T., Bryan, G. L., & Norman, M. L. 2002, Sci, 295, 93
Aubert, D., Pichon, C., & Colombi, S. 2004, MNRAS, 352, 376
Barai, P., & de Gouveia Dal Pino, E. M. 2018, arXiv:1807.04768
Beers, T. C., & Christlieb, N. 2005, ARA&A, 43, 531
Bose, S., Deason, A. J., & Frenk, C. S. 2018, ApJ, 863, 123
Bouwens, R. J., Illingworth, G. D., Oesch, P. A., et al. 2015, ApJ, 803, 34
Bromm, V., Coppi, P. S., & Larson, R. B. 1999, ApJL, 527, L5
Bromm, V., Coppi, P. S., & Larson, R. B. 2002, ApJ, 564, 23
Bromm, V., Ferrara, A., Coppi, P. S., & Larson, R. B. 2001, MNRAS, 328, 969
Brook, C. B., Kawata, D., Scannapieco, E., Martel, H., & Gibson, B. K. 2007, ApJ, 661, 10
Cassata, P., Le Fèvre, O., Charlot, S., et al. 2013, A&A, 556, A68
Castellani, V., Chieffi, A., & Tornambe, A. 1983, ApJ, 272, 249
Clark, P. C., Glover, S. C. O., Klessen, R. S., & Bromm, V. 2011, ApJ, 727, 110
Colombi, S. 2013, AdaptaHOP: Subclump Finder, Astrophysics Source Code Library, ascl:1305.004
Couchman, H. M. P., & Rees, M. J. 1986, MNRAS, 221, 53
de Bennassuti, M., Salvadori, S., Schneider, R., Valiante, R., & Omukai, K. 2017, MNRAS, 465, 926
Deharveng, L., Schuller, F., Anderson, L., et al. 2010, A&A, 523, A6
Dopcke, G., Glover, S. C. O., Clark, P. C., & Klessen, R. S. 2011, ApJL, 729, L3
Dopcke, G., Glover, S. C. O., Clark, P. C., & Klessen, R. S. 2013, ApJ, 766, 103
Dubois, Y., & Teyssier, R. 2008, A&A, 477, 79
El Eid, M. F., Fricke, K. J., & Ober, W. W. 1983, A&A, 119, 54
Ferland, G., van Hoof, P., Verner, D., et al. 1999, Cloudy: Numerical Simulation of Plasmas and Their Spectra, Astrophysics Source Code Library, ascl:9910.001
Finkelstein, S. L. 2016, PASA, 33, e037
Frebel, A., Aoki, W., Christlieb, N., et al. 2005, Natur, 434, 871
Frebel, A., & Norris, J. E. 2015, ARA&A, 53, 631
Freeman, K., & Bland-Hawthorn, J. 2002, ARA&A, 40, 487
Furlanetto, S. R., & Oh, S. P. 2008, ApJ, 682, 14
Gardner, J. P., Mather, J. C., Clampin, M., et al. 2006, SSRv, 123, 485
Haardt, F., & Madau, P. 1996, ApJ, 461, 20
Hahn, O., & Abel, T. 2013, MUSIC: MUlti-Scale Initial Conditions, Astrophysics Source Code Library, ascl:1311.011
Hartwig, T., Bromm, V., Klessen, R. S., & Glover, S. C. O. 2014, MNRAS, 447, 3892
Hartwig, T., Bromm, V., Klessen, R. S., & Glover, S. C. O. 2015, MNRAS, 447, 3892
Hartwig, T., Yoshida, N., Magg, M., et al. 2018, MNRAS, 478, 1795
Heger, A. 2018, STARFIT, http://starfit.org/
Heger, A., Fryer, C. L., Woosley, S. E., Langer, N., & Hartmann, D. H. 2003, ApJ, 591, 288
Heger, A., & Woosley, S. E. 2002, ApJ, 567, 532
Heger, A., & Woosley, S. E. 2010, ApJ, 724, 341
Hirano, S., & Yoshida, N. 2013, ApJ, 763, 52
Ishigaki, M. N., Tominaga, N., Kobayashi, C., & Nomoto, K. 2018, ApJ, 857, 46
Jaacks, J., Thompson, R., Finkelstein, S. L., & Bromm, V. 2018, MNRAS, 475, 4396
Jeon, M., Pawlik, A. H., Greif, T. H., et al. 2012, in AIP Conf. Ser. 1480, ed. M. Umemura & K. Omukai (Melville, NY: AIP), 325
Johnson, J. L. 2010, MNRAS, 404, 1425
Johnson, J. L., & Bromm, V. 2006, MNRAS, 366, 247
Johnson, J. L., Vecchia, C. D., & Khochfar, S. 2013, MNRAS, 428, 1857
Kashikawa, N., Nagao, T., Toshikawa, J., et al. 2012, ApJ, 761, 85
Keller, S. C., Bessell, M. S., Frebel, A., et al. 2014, Natur, 506, 463
Kitayama, T., & Yoshida, N. 2005, ApJ, 630, 675
Komatsu, E., Dunkley, J., Nolta, M., et al. 2009, ApJS, 180, 330
Larson, R. B. 1973, MNRAS, 161, 133
Leitherer, C., Ekström, S., Meynet, G., et al. 2014, ApJS, 212, 14
Loeb, A. 2010, How Did the First Stars and Galaxies Form? (Princeton, NJ: Princeton Univ. Press)
Mackey, J., Bromm, V., & Hernquist, L. 2003, ApJ, 586, 1
Madau, P. 1995, ApJ, 441, 18
Madau, P., & Dickinson, M. 2014, ARA&A, 52, 415

Martin, P., Schwarz, D., & Mandy, M. 1996, ApJ, 461, 265
Mason, C. A., Trenti, M., & Treu, T. 2015, ApJ, 813, 21
McLeod, D. J., McLure, R. J., Dunlop, J. S., et al. 2015, MNRAS, 450, 3032
Nagao, T., Sasaki, S. S., Maiolino, R., et al. 2008, ApJ, 680, 100
Nomoto, K., Kobayashi, C., & Tominaga, N. 2013, ARA&A, 51, 457
Norman, M. L. 2010, in AIP Conf. Ser. 1294, ed. D. J. Whalen, V. Bromm, & N. Yoshida (Melville, NY: AIP), 17
Oesch, P. A., Bouwens, R. J., Illingworth, G. D., et al. 2013, ApJ, 773, 75
Oesch, P. A., Bouwens, R. J., Illingworth, G. D., et al. 2015, ApJ, 808, 104
Omukai, K., Tsuribe, T., Schneider, R., & Ferrara, A. 2005, ApJ, 626, 627
O'Shea, B. W., & Norman, M. L. 2007, ApJ, 654, 66
O'Shea, B. W., Wise, J. H., Xu, H., & Norman, M. L. 2015, ApJL, 807, L12
Pallottini, A., Ferrara, A., Gallerani, S., Salvadori, S., & D'Odorico, V. 2014, MNRAS, 440, 2498
Pan, L., & Scannapieco, E. 2010, ApJ, 721, 1765
Pan, L., Scannapieco, E., & Scalo, J. 2012, JFM, 700, 459
Pan, L., Scannapieco, E., & Scalo, J. 2013, ApJ, 775, 111
Panagia, N., Stiavelli, M., Ferguson, H., & Stockman, H. S. 2003, RMxAC, 27, 17, 230
Planck Collaboration, Ade, P. A. R., Aghanim, N., et al. 2016, A&A, 594, A13
Pontzen, A., Roškar, R., Stinson, G., & Woods, R. 2013, pynbody: N-Body/SPH Analysis for Python, Astrophysics Source Code Library, ascl:1305.002
Prieto, J., Escala, A., Volonteri, M., & Dubois, Y. 2017, ApJ, 836, 216
Prieto, J. P., Infante, L., & Jimenez, R. 2008, arXiv:0809.2786
Raiter, A., Schaerer, D., & Fosbury, R. A. E. 2010, A&A, 523, A64
Rasera, Y., & Teyssier, R. 2006, A&A, 445, 1
Reed, D. S., Bower, R., Frenk, C. S., et al. 2005, MNRAS, 363, 393
Ritter, C., Côté, B., Herwig, F., Navarro, J. F., & Fryer, C. L. 2018a, ApJS, 237, 42
Ritter, C., Côté, B., Herwig, F., Navarro, J. F., & Fryer, C. 2018b, SYGMA: Modeling Stellar Yields for Galactic Modeling, Astrophysics Source Code Library, ascl:1806.019
Rosen, A., & Bregman, J. N. 1995, ApJ, 440, 634
Salpeter, E. E. 1955, ApJ, 121, 161
Salvadori, S., Ferrara, A., Schneider, R., Scannapieco, E., & Kawata, D. 2010, MNRAS, 401, L5
Sarmento, R., Scannapieco, E., & Cohen, S. 2018, ApJ, 854, 75
Sarmento, R., Scannapieco, E., & Pan, L. 2017, ApJ, 834, 23
Scannapieco, E., Madau, P., Woosley, S., Heger, A., & Ferrara, A. 2005, ApJ, 633, 1031
Scannapieco, E., & Oh, S. P. 2004, ApJ, 608, 62
Scannapieco, E., Schneider, R., & Ferrara, A. 2003, ApJ, 589, 35
Schaerer, D. 2002, A&A, 382, 28
Schmidt, M. 1959, ApJ, 129, 243
Schneider, R., Omukai, K., Bianchi, S., & Valiante, R. 2012, MNRAS, 419, 1566
Simpson, C. M., Bryan, G. L., Johnston, K. V., et al. 2013, MNRAS, 432, 1989
Smidt, J., Whalen, D. J., Wiggins, B. K., et al. 2014, ApJ, 797, 97
Sobral, D., Matthee, J., Darvish, B., et al. 2015, ApJ, 808, 139
Somerville, R. S., Hopkins, P. F., Cox, T. J., Robertson, B. E., & Hernquist, L. 2008, MNRAS, 391, 481
Stacy, A., & Bromm, V. 2013, MNRAS, 433, 1094
Stacy, A., & Bromm, V. 2014, ApJ, 785, 73
Stacy, A., Greif, T. H., & Bromm, V. 2010, MNRAS, 403, 45
Susa, H. 2013, ApJ, 773, 185
Susa, H., Hasegawa, K., & Tominaga, N. 2014, ApJ, 792, 32
Teyssier, R. 2002, A&A, 385, 337
Teyssier, R. 2010, RAMSES: A New N-body and Hydrodynamical Code, Astrophysics Source Code Library, ascl:1011.007
The yt project, 2010, yt: A Multi-Code Analysis Toolkit for Astrophysical Simulation Data, Astrophysics Source Code Library, ascl:1011.022
Tornatore, L., Ferrara, A., & Schneider, R. 2007, MNRAS, 382, 945
Tremblin, P., Audit, E., Minier, V., Schmidt, W., & Schneider, N. 2012, A&A, 546, A33
Trenti, M., & Stiavelli, M. 2008, ApJ, 676, 767
Tumlinson, J. 2006, ApJ, 641, 1
Tumlinson, J., Giroux, M. L., & Shull, J. M. 2001, ApJL, 550, L1
Tumlinson, J., & Shull, J. M. 2000, ApJL, 528, L65
Turk, M. J., Abel, T., & O'Shea, B. 2009, Sci, 325, 601
Whalen, D., Abel, T., & Norman, M. L. 2004, ApJ, 610, 14
Whalen, D., van Veelen, B., O'Shea, B. W., & Norman, M. L. 2008, ApJ, 682, 49
Whalen, D. J. 2012, in AIP Conf. Proc. 1480, ed. M. Umemura & K. Omukai (Melville, NY: AIP), 194
Whalen, D. J., Joggerst, C. C., Fryer, C. L., et al. 2013, ApJ, 768, 95
Windhorst, R. A., Timmes, F. X., Wyithe, J. S. B., et al. 2018, ApJS, 234, 41
Wise, J. H., Turk, M. J., Norman, M. L., & Abel, T. 2011, ApJ, 745, 50
Woosley, S. E., Heger, A., & Weaver, T. A. 2002, RvMP, 74, 1015
Xu, H., Norman, M. L., O'Shea, B. W., & Wise, J. H. 2016a, ApJ, 823, 140
Xu, H., Wise, J. H., Norman, M. L., Ahn, K., & O'Shea, B. W. 2016b, ApJ, 833, 84
Yoon, J., Beers, T. C., Dietz, S., et al. 2018, ApJ, 861, 146
Yoon, J., Beers, T. C., Placco, V. M., et al. 2016, ApJ, 833, 20